Materials Horizons

Accepted Manuscript

ROYAL SOCIETY OF CHEMISTRY

rsc.li/materials-horizons

Journal Name ARTICLE

Advancements in All-Solid-State Hybrid Solar Cells Based on Organometal Halide Perovskite

Cite this: DOI: 10.1039/x0xx00000x

Shaowei Shi[a,b], Yongfang Li[c], Xiaoyu Li [a,b]*, and Haiqiao Wang [a,b]*

Received 00th January 2012,
Accepted 00th January 2012

DOI: 10.1039/x0xx00000x

www.rsc.org/

Over the past several years, organic−inorganic hybrid perovskites have gained considerable research attention due to the direct band gap, large absorption coefficient, ambipolar diffusion and long carrier diffusion length, and have revolutionized the prospects of emerging photovoltaic technologies, with the highest power conversion efficiency of over 19% achieved under laboratory conditions. In this perspective, we summarize the recent development in perovskite solar cells (from **April 2009** to **December 2014**), describe the unique properties of organometal halide perovskites leading to their rapid emergence, and discuss challenges such as stability and environmental issues to be faced in the future.

CONTENTS

Nomenclature	
3-D	three-dimensional
ALD	atomic layer deposition
AZO	Al-doped mesoporous ZnO
BCP	bathocuproine
BHJ	bulk-heterojunction
Bphen	bathophenanthroline
C60	fullerene
CBD	chemical bath deposition
CE	counter electrode
DIO	1,8-diiodooctane
DMF	N, N –dimethylformamide
DMSO	dimethylsulfoxide
DP	deposition process
DSSC	dye sensitized solar cell
DSVD	dual source vacuum deposition
ETM	electron-transporting material
FA	formamidinium
FF	fill factor
FG	flaky graphite
FK102	tris(2-(1H-pyrazol-1-yl)pyridine)cobalt(III) tris(hexafluorophosphate)
FK209	tris(2-(1H-pyrazol-1-yl)-4-tert-butylpyridine)cobalt(III) tris(bis(trifluoromethylsulfonyl)imide)
FK269	bis(2,6-di(1H-pyrazol-1-

	yl)pyridine)cobalt(III) tris(bis(trifluoromethylsulfonyl)-imide)
FTO	fluorine-doped tin oxide
GBL	γ-butyrolactone
GO	graphene oxide
HI	hydroiodic acid
HMTA	hexamethylenetetramine
HMTA	hexamethylenetetramine
HTM	hole-transporting material
IC60BA	indene-C_{60} bisadduct
IPCE	incident photon-to-electron conversion efficiency
IPFB	iodopentafluorobenzene
IQE	internal quantum efficiency
ITO	indium tin oxide
*J*sc	short-circuit current density
LiTFSI	bis(trifluoromethane)sulfonimide lithium salt
MMOPSC	mesoporous metal oxide perovskite solar cell
MSSC	meso-superstructured solar cell
NRA	nanorod array
OPV	organic photovoltaic cell
OSPD	one step precursor deposition
PA	phenylamine
PA	phenylamine
PC60BM	[6,6]-phenyl C61-butyric acid methyl ester
PC70BM	[6,6]-phenyl C71-butyric acid methyl ester
PCE	power conversion efficiency
PDMS	polydimethylsiloxane
PECVD	plasma-enhanced chemical vapor deposition
PEIE	polyethyleneimine ethoxylated
PET	polyethylene terephthalate
PFI	perfluorinated ionomer
PHJ	planar heterojunction
PHJPSC	planar heterojunction perovskite solar cell
PL	perovskite layer
PMMA	poly(methyl methacrylate)
Poly-TPD	poly(N,N′-bis(4-butylphenyl)-N,N′-bis(phenyl)benzidine)
PT	polythiophene
PTAA	poly(-triarylamine)
QDSC	quantum dot solar cell
R_s	series resistance
R_{sh}	shunt resistance
SCD	spray-coating deposition
SDP	sequential deposition process
SG	spheroidal graphite
spiro-OMeTAD *or* spiro	,2',7,7'-tetrakis(N,N-di-p-methoxyphenylamine)-9,9'-spirobifluorene
ss-DSSCs	solid-state dye-sensitized solar cells
SVD	sequential vapour deposition
SWNTs	single-walled carbon nanotubes
TAA	triarylamine
TBP	4-tert-butylpyridine
TPA	triphenylamine
TSSD	two step spin-coating deposition
VASP	vapor assisted solution process
*V*oc	open-circuit voltage

1. Introduction

Increasing energy demands and concerns about global warming drive the exploration/development of clean, inexpensive and renewable energy sources. Several new energy technologies for converting solar energy to electricity, including organic photovoltaic cells (OPVs), dye sensitized solar cells (DSSCs) and quantum dot solar cells (QDSCs) have attracted significant attention as low-cost alternatives to conventional silicon-based solar cells. Recently, the hybrid organometal halide perovskites, which were initially employed in DSSCs as light absorbers, have gradually become one of the most important active materials for all-solid-state solid cells (which can be named as perovskite solar cells) due to their direct band gap, large absorption coefficient, ambipolar diffusion and long carrier diffusion length, with the highest efficiency of up to ~20%. Two important journals, *Science*[1] and *Nature*[2], both highlighted perovskite photovoltaics as one of the biggest breakthroughs of the year 2013.[3]

"Perovskite", which is named after the Russian mineralogist, L. A. Perovski (1792–1856), is defined as one class of compounds which crystallise in the ABX_3 structure (e.g. $CaTiO_3$).[4] An ideal perovskite structure has a cubic $Pm\bar{3}m$ crystal structure, which consists of a three-dimensional (3-D) framework of corner-sharing BX_6 octahedron with the A ion placed in the cuboctahedral interstices, as shown in Figure 1. In the case of the organometal trihalide perovskites, A is an organic cation (typically $CH_3NH_3^+$ or $HN{=}CHNH_3^+$), B is a metal cation (typically Sn^{2+} or Pb^{2+}), and X is a halide anion (typically Cl^-, Br^- or I^-). Goldschmidt's tolerance factor (t), $t = (R_A + R_X)/[2^{1/2}(R_B + R_X)]$, (where R_A, R_B and R_X are the ionic radii for the ions in the A, B and X sites, respectively; t=1 corresponds to a perfectly packed perovskite structure) and octahedral factor (μ), $\mu = R_B/R_X$, can be used to estimate the stability and distortion of the perovskite structure.[5-7]

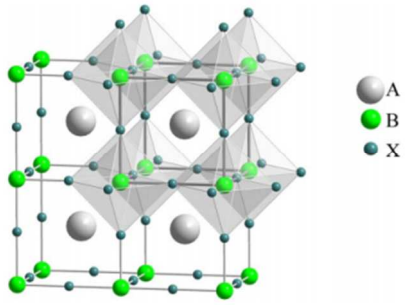

Fig. 1. The basic perovskite structure (ABX_3). Reprinted with permission.[7]

In the present paper, we aim to offer a brief review on the application of hybrid organic–inorganic perovskites (typically methylammonium lead halide perovskite) in different photovoltaic devices, including the mesoporous metal oxide solar cell, meso-superstructured solar cell and planar heterojunction solar cell. Although great progress has been achieved in the past three years, continued development of perovskite solar cell will require a better understanding of the relationships between perovskite structure, device architecture, hole/electron conductor, and device performance than is currently available.

2. Progress in hybrid organic–inorganic perovskite solar cells

Since O'Regan and Grätzel firstly introduced the conception of DSSCs in 1991,[8] in the following two decades, DSSCs have drawn great attention both in scientific and technological aspects and are considered to be a potential alternative to conventional inorganic silicon-based solar cells due to the low processing costs and inexpensive constituent materials. Generally, a DSSC contains a transparent conducting oxide electrode (typically fluorine-doped tin oxide (FTO) or indium-doped tin oxide (ITO)), a dye-sensitized mesoporous semiconductor metal oxide (typically nanocrystalline TiO_2) film, a platinum (Pt) counter electrode, and an electrolyte containing redox couples (typically I^-/I^{3-}) dissolved in a solvent. However, although power conversion efficiencies (PCEs) of close to 13% have been achieved with this device architecture[9], such cells suffer from potential leakage problems associated with the corrosive and volatile nature of the liquid electrolyte and, thus, may be impractical for large-scale applications. In 1998, the first example of solid-state dye-sensitized solar cells (ss-DSSCs) emerged by using a solid hole-transporting material (HTM) 2,2',7,7'-tetrakis(N,N-di-p-methoxyphenylamine)-9,9'-spirobifluorene (**spiro-OMeTAD** or **spiro**) instead of the conventional liquid redox electrolyte.[10] With this change, ss-DSSCs appeared to be quickly becoming both efficient and stable. Nevertheless, in the following a long period of time, this type of cell did not reach the predetermined level of high efficiencies, yielding a maximum PCE of 7.2% based on tris(2-(1H-pyrazol-1-yl)pyridine)cobalt(III) doped **spiro-OMeTAD** and a high molar extinction coefficient organic photosensitizer.[11]

The real breakthrough of ss-DSSCs came in 2012, when Grätzel et al[12] and Snaith et al[13] independently employed $CH_3NH_3PbI_3$ ($MAPbI_3$) and $CH_3NH_3PbI_2Cl$ ($MAPbI_2Cl$) perovskite nanocrystals as ligth harvesters using submicron thick mesoporous TiO_2 film and **spiro-MeOTAD** as an electron- and a hole-transporting layer. PCEs of 9.7% and 7.6% were achieved under AM 1.5G illumination along with excellent long term stability. Moreover, by replacing the *n*-type mesoporous TiO_2 with insulating mesoporous Al_2O_3, an evolution of the ss-DSSC, which is termed as the meso-superstructured solar cell (MSSC) was developed by Snaith et al.[13] FTO/blocking layer (bl)-TiO_2/mesoporous (mp)-Al_2O_3/$MAPbI_2Cl$/**spiro-OMeTAD**/Ag-based device showed a PCE of 10.9%[13]. Etgar and coworkers also fabricated a hole conductor-free $MAPbI_3$/mp-TiO_2 heterojunction solar cell (FTO/bl-TiO_2/mp-TiO_2/$MAPbI_3$/Au) and achieved a PCE of 5.5%.[14] All above mentioned proved that this organometal halide perovskite can not only play as an absorber (dye) but also as an ambipolar charge transporter, indicating the possibility for applying in various device architectures.

Actually, early in 2009, organometal halide perovskites $MAPbBr_3$ and $MAPbI_3$ have been initially attempted in conventional liquid electrolyte-based DSSCs, yielding PCEs of 3.13% and 3.81%, respectively (see Figure 2).[15] Later, in 2011, *via* optimization of the titania surface and perovskite ($MAPbI_3$) processing, Park and coworkers further improved the PCE to 6.54% in a perovskite quantum dot-sensitized 3.6 μm -thick TiO_2 film under AM 1.5G 1 sun illumination.[16] The authors also reported a $(CH_3CH_2NH_3)PbI_3$ -sensitized solar cell with iodide-based redox electrolyte and achieved a PCE of 2.4%.[17] These pioneering work opened the prelude of organometal halide perovskites to be applied as active layers in ss-DSSCs. However, electrolyte-based devices were usually unstable and performance degraded rapidly due to the dissolution or decomposition of perovskite in liquid electrolyte.

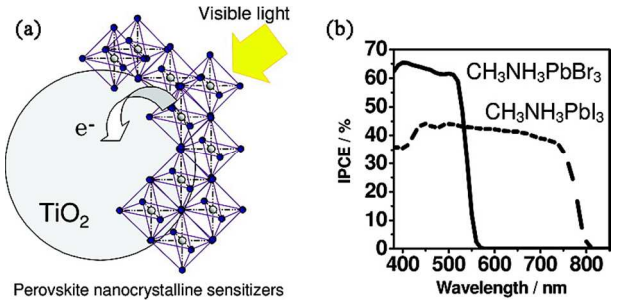

Fig. 2. (a) The schematic of perovskite-sensitized TiO_2 undergoing photoexcitation and electron transfer. (b) The incident photon-to-electron conversion efficiency (IPCE) spectra for $MAPbBr_3$/$MAPbI_3$-sensitized solar cells. Reprinted with permission.[15]

After the breakthrough work of ss-DSSCs based on organometal halide perovskites[12,13], in 2013, two papers published in the journal *Nature* lift the study of perovskite solar cells to a new level.[18,19] First, by using sequential deposition process to fabricate $MAPbI_3$ films, a remarkable PCE of 15% was measured in a FTO/bl-TiO_2/mp-TiO_2/$MAPbI_3$/**spiro-OMeTAD**/Au-based device.[18] Subsequently, Snaith and coworkers deposited a high-quality $MAPbI_{3-x}Cl_x$ film *via* dual source vacuum deposition in a planar heterojunction (PHJ) perovskite solar cell (FTO/bl-TiO_2/$MAPbI_{3-x}Cl_x$/**spiro-OMeTAD**/Ag) and achieved a PCE of 15.4%.[19] Seok and coworkers also obtained a PCE of 12% in a FTO/bl-TiO_2/mp-TiO_2/$MAPbI_3$/**PTAA**/Au-based device by replacing the conventional **spiro-OMeTAD** HTM with poly(-triarylamine) (**PTAA**).[20] Since then, follow-up works such as the morphology and crystal optimization, HTM/ETM (electron-transporting material) adjustment and interface/band-gap engineering further improved the device performance to nearly 20% efficiency, opening up a new direction for developing highly efficient solar cells with a low cost and good stability.

At present, two type perovskite solar cells, which based on a porous or planar architecture, are the focuses of research. It is worth pointing out that in a porous device, mesoporous "scaffold" can not only be conductors (e.g. TiO_2, ZnO, NiO) but also be insulators (e.g. Al_2O_3, ZrO_2, SiO_2). For the purposes of distinguishing these two type devices, herein, we separate this porous device into two groups, including mesoporous metal oxide perovskite solar cell (MMOPSC) (with mesoporous conductors) and the above-mentioned MSSC (with mesoporous

insulators). So far the highest PCEs achieved from MMOPSC, MSSC and planar heterojunction perovskite solar cell (PHJPSC) are 17.01%[21], 15.9%[22] and 19.3%[23], respectively.

3. Deposition processes for perovskite films

As the core part of perovskite solar cells, the morphology and crystal structure of perovskite absorbers are important for achieving high-performance devices. So far seven main deposition methods have been reported including: one step precursor deposition (OSPD), sequential deposition process (SDP), two step spin-coating deposition (TSSD), dual source vacuum deposition (DSVD), sequential vapour deposition (SVD), vapour-assisted solution process (VASP) and spray-coating deposition (SCD). Among the above mentioned methods, devices fabricated using OSPD, SDP, TSSD, DSVD or SVD have yielded PCEs of over 15%, while PCEs of over 10% have been achieved using VASP or SCD.

3.1 Solution-based deposition methods (OSPD, SDP, TSSD, SCD)

Initial report of one step precursor deposition for organo-lead halide perovskite solar cell was from Miyasaka and coworkers in 2009, by spin-coating a precursor solution containing MAX and PbX_2 (X = Br, I) on the mp-TiO_2 layer to form $MAPbBr_3$ or $MAPbI_3$ nanocrystalline.[15] For the widely studied $MAPbI_3$ or $MAPbI_{3-x}Cl_x$-based perovskite solar cells, γ-butyrolactone (GBL) and N, N –dimethylformamide (DMF) are commonly used solvents for dissolving PbX_2 (X = I, Cl) and MAI, in which the mole ration of MAI and PbI_2 is 1:1 while the MAI and $PbCl_2$ are in a molar ratio of 3 : 1. Generally, the perovskite precursor solution (~40 wt%) is firstly stirred at a certain temperature (eg. 80 ^oC) overnight before spin-coated on the substrate. Then a thermal annealing (~100 ^oC) is processed to remove the solvent and complete transformation of the precursor to the resulting perovskite crystalline. The thickness of the perovskite film is tuned by changing the precursor concentration and/or spin speed of the perovskite precursor solution. The problem in this deposition method is the uncontrolled crystallization process of the perovskite, which always results in a wide spread of photovoltaic performance and low reproducibility in the resulting devices (especially for porous structure-based devices). To avoid the large perovskite grains and uncovered pin-hole areas, follow-up morphology optimizations such as solvent-engineering technology (eg. using a mixed solvent or fast crystallization-deposition),[24-30] thermal annealing,[31-34] and additive treatment (eg. 1,8-diiodooctane (DIO), NH_4Cl and MACl)[35-38] have been reported by several groups and achieved excellent efficiencies. To date, OSPD is still considered as one of the most simple and important deposition methods, and the record efficiency (19.3%) of perovskite solar cells was achieved *via* this approach.[23]

Another important solution-based deposition is sequential deposition process, which was originally introduced by Mitzi et al in 1998,[39] then employed in perovskite solar cells by Grätzel et al in 2013.[18] In this process, a PbX_2 (X = I, Cl[40]) solution in DMF (or dimethylsulphoxide (DMSO)[41]) is first spin-coated (one or more times[42]) on the top of porous or planar substrates, followed by dipping it into a solution of MAI in 2-propanol (seconds to tens of minutes) to transform into the perovskite. The perovskite crystal size and orientation on the substrate can be controlled by modifying the prewetting time of 2-propanol or reaction temperature in the second step. [43-45] So far, using this deposition, perovskite solar cells based on mesoporous metal oxide, meso-superstructured or planar structures have achieved the highest PCE of 15%,[18] 10.8%[46] and 15.7%[47], respectively. Compared with OSPD, SDP is more beneficial to improve the coverage, pore-filling, and morphology of the deposited perovskite in porous substrates, therefore further improves the device performance. However, for most PHJ perovskite solar cells, SDP cannot perform as successfully as in nanostructured devices. Without the porous "scaffold", it is hard for MAI to penetrate into the PbX_2 films due to the limited reaction interface area, leading to a long reaction time and/or low conversion rate of PbX_2.[48] Also, large randomly distributed grains always appear during the quick crystallization of perovskite, which result in a very rough perovskite film and low efficiency.[49]

In 2014, Huang and coworkers reported an efficient planar perovskite solar cell (PCE = 15.4%) using a two step spin-coating deposition method, [49] in which the solution of PbI_2 in DMF and the solution of MAI in 2-propanol were spin-coated step by step on the ITO/PETDOT: PSS-based substrate at first, followed by thermal annealing at 100 ^oC to drive the interdiffusion of precursors (this step can be skipped *via* well-controlling the thickness of PbI_2 and the process of adding MAI[50]). Later, Park et al found that the size of the $MAPbI_3$ cuboids was very strongly dependent on MAI concentration and the exposure time of the PbI_2 to the MAI solution before spin coating, and high PCE of 17.01% was achieved using this modified TSSD.[21,51] Lidzey et al explored the use of ultra-sonic spray-coating as a deposition technique to create $MAPbI_{3-x}Cl_x$ perovskite thin-films in ambient conditions.[52] Precursor solution of MAI and $PbCl_2$ (3 : 1 molar ratio) in DMF or DMSO was deposited on the substrates from a single pass of the spray-head, then transformed into $MAPbI_{3-x}Cl_x$ through thermal annealing. Planar device with a ITO/PEDOT:PSS/$MAPbI_{3-x}Cl_x$/[6,6]-phenyl C61-butyric acid methyl ester (**PC60BM**)/Ca/Al structure yielded a PCE of 11.1% with an average efficiency of 7.8%, which was comparable to the devices fabricated *via* spin-coating, showing the commercial potential of SCD used in the large-area, low-cost, efficient manufacture of perovskite solar cells.

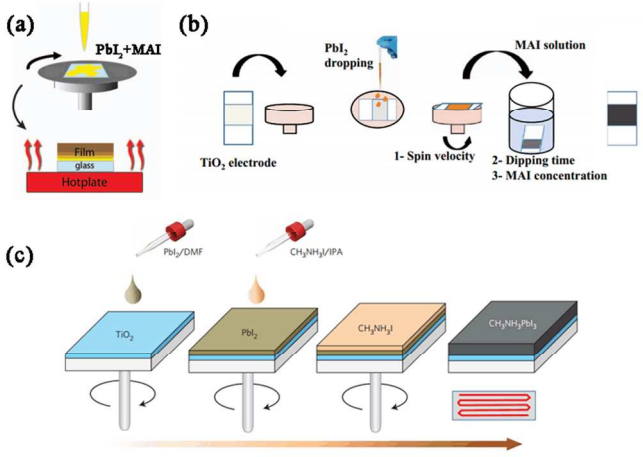

Fig. 3. Solution-based deposition methods (e.g. $MAPbI_3$). (a) One step precursor deposition (OSPD). Reprinted with permission.[53] (b) Sequential deposition process (SDP). Reprinted with permission[54]; (c) Two step spin-coating deposition (TSSD). Reprinted with permission.[21]

3.2 Vapor-based deposition methods (DSVD, SVD, VASP)

Compared with solution-based deposition processes (especially OSPD and SDP), vapor-based deposition processes are not used as commonly as the former technologies, mainly due to the increasing manufacturing cost. In 2013, Snaith and coworkers initially fabricated a $MAPbI_{3-x}Cl_x$-based PHJ perovskite solar cell (FTO/bl-TiO_2/$MAPbI_{3-x}Cl_x$/**spiro-OMeTAD**/Ag) *via* dual source vacuum deposition and achieved a high PCE of 15.4%.[19] In this process, MAI and $PbCl_2$ were evaporated simultaneously from separate sources and a superior uniformity of the perovskite films was observed over a range of length scales. Subsequently, using DSVD, Bolink and Sarkar groups reported three type PHJ devices based on ITO/PEDOT:PSS/**Poly-TPD**/$MAPbI_3$/**PC60BM**/Au, FTO/NiO/$MAPbI_{3-x}Cl_x$/**PC60BM**/Ag and FTO/CuSCN/$MAPbI_{3-x}Cl_x$/**PC60BM**/Ag, yielding PCEs of 14.8%, 7.26%, and 3.8%, respectively.

In 2014, Cui[55] and Lin[56] et al developed a sequential vapor deposition process, in which PbX_2 (X = I, Cl) and MAI is vapour-deposited on the substrates layer by layer. PbX_2 reacts with MAI *in situ*, followed by a thermal annealing to complete the perovskite crystal transformation. This deposition process is very similar with the above mentioned precursor interdiffusion deposition method (TSSD), except the SVD uses vapor deposition. Compared with the perovskite films fabricated *via* DSVD, SVD fabricated films demonstrate larger crystal domain size, which is beneficial to improve carriers-transport properties. Also, SVD enhances the control on the perovskite morphology by independent manipulation of PbX_2 and MAI. Using SVD, Cui and coworkers prepared a uniform, smooth $MAPbI_3$ film and fabricated an easy planar perovskite solar cell consisting of only a $MAPbI_3$/fullerene (**C60**) layer sandwiched between two electrical contacts.[55] No hole conductor (e.g. PEDOT:PSS or NiO_x) was needed in this system and a PCE of 5.4% was achieved under AM1.5G one sun illumination. Lin et al also achieved a high PCE of 15.4% in an ITO/PEDOT:PSS/$MAPbI_{3-x}Cl_x$/**C60**/bathophenanthroline (Bphen)/Ca/Ag-based device.[56]

Yang and coworkers reported a blended deposition method called vapour-assisted solution process to fabricate $MAPbI_3$ films.[48] First, the solution of PbI_2 in DMF was spin-coated on the FTO/bl-TiO_2 substrates, and dried at 110 °C for 15 min. Then the PbI_2-coated substrates were annealed in MAI vapor at 150 °C in N_2 atmosphere for desired time to form the perovskite films. After cooling down, the as-prepared substrates were washed with isopropanol, dried and annealed to complete the deposition. The perovskite film derived from this approach exhibited full surface coverage, uniform grain structure with grain size up to micrometers, and ~100% precursor transformation completeness. PHJ device based on FTO/bl-TiO_2/$MAPbI_{3-x}Cl_x$/**spiro-OMeTAD**/Ag yielded a PCE of 12.1%. Later, *via* VASP, the authors introduced a controllable self-induced passivation technique by tuning the amount of PbI_2 species in perovskite grain boundaries and at the relevant interfaces, which was helpful for understanding the carrier behavior along the heterojunctions and the polycrystalline nature of hybrid perovskite thin films.[57-59]

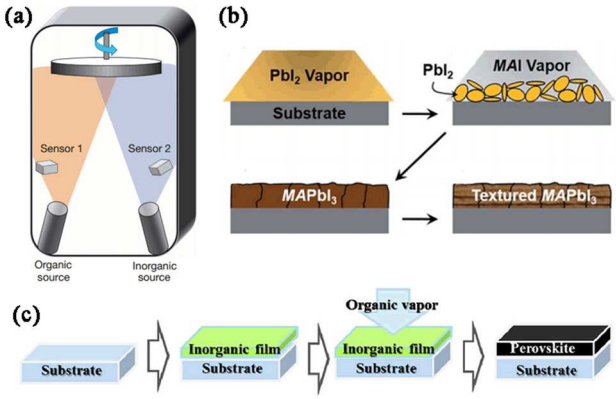

Fig. 4. Vapor-based deposition methods. (a) Dual source vacuum deposition (DSVD). Reprinted with permission.[19] (b) Sequential vapour deposition (SVD) (e.g. $MAPbI_3$). Reprinted with permission.[55] (c) Vapor assisted solution process (VASP). Reprinted with permission.[48]

Table 1. Optimal device performance reported so far *via* different perovskite deposition meathods and corresponding device configurations

Deposition Process (DP)	Device structure	*J*sc (mA/cm^2)	*V*oc (V)	FF (%)	PCE (%)	Ref.
OSPD	ITO/PEIE/bl-TiO_2(Y)/$MAPbI_{3-x}Cl_x$/**spiro**/Au	22.75	1.13	75.01	19.3	23
SDP	ITO/bl-ZnO/$MAPbI_3$/**spiro**/Ag	20.4	1.03	74.9	15.7	47
TSSD	ITO/bl-TiO_2/mp-TiO_2/$MAPbI_3$/**spiro**/Au	21.64	1.056	74.1	17.01	21
DSVD	FTO/bl-TiO_2/$MAPbI_{3-x}Cl_x$/**spiro**/Ag	21.5	1.07	67	15.4	19
SVD	ITO/PEDOT:PSS/$MAPbI_{3-x}Cl_x$/**C60**/Bphen/Ca/Ag	20.9	1.02	72.2	15.4	56
VASP	FTO/bl-TiO_2/$MAPbI_{3-x}Cl_x$/**spiro**/Ag	19.8	0.924	66.3	12.1	48
SCD	ITO/PEDOT:PSS/$MAPbI_{3-x}Cl_x$/**PC60BM**/Ca/Al	16.8	0.92	72	11.1	52

4. Device architectures of perovskite solar cells

4.1 Mesoporous metal oxide -based perovskite solar cells

4.1.1 Device based on mesoporous *n*-type TiO_2

As the most common device architecture for perovskite solar cells, devices based on a perovskite sensitized mesoporous TiO_2 scaffold have yielded PCEs from 9.7%[12] to over 16%[21,24,60]. This porous *n*-type TiO_2 film not only extracts photoexcited electrons generated in the absorber layer[61] but also increases the perovskite crystal transformation when the perovskite layer is fabricated using SDP.[62] For a typical mesoporous TiO_2 -based perovskite solar cell, the fabrication process always starts with the deposition of a compact TiO_2 layer on the top of pre-cleaned FTO conductive substrates. Three strategies are widely used at present for depositing the compact TiO_2 layer, which acts as a blocking layer to prevent

direct contact between FTO and the infiltrated HTM layer, including 1) spin-coating the colloidal dispersion of TiO_2 nanoparticles followed by a thermal treatment (titanium source: $TiCl_4$, [22] titanium isopropoxide,[63 64] tetra-n-butyl-titanate[65]); 2) spin-coating titanium precursor solutions followed by a thermal treatment (titanium source: $TiCl_4$[66], titanium isopropoxide[67], titanium diisopropoxide bis(acetylacetonate)[12]); 3) spray pyrolysis deposition (titanium source: titanium diisopropoxide bis(acetylacetonate)[18]). Also, other methods such as atomic layer deposition (ALD)[68-70] or thermal oxidation of Ti film[71,72] were also reported. Then a mesoporous *n*-type TiO_2 layer is constructed by spin-coating, screen-printing or doctor-blading the TiO_2 nanoparticle paste on the top of the compact TiO_2 layers followed by sintering. After that, OSPD or SDP is employed to deposit the hybrid organic–inorganic perovskite on the mesoporous TiO_2 films. Then the organic or inorganic HTM layer is deposited on the top of the perovskite layer (the existence of HTMs not only favours the hole transport but also blocks the electron transfer from perovskites to the electrode). This step can be skipped in a HTM-free mp-TiO_2/perovskite heterojunction solar cell.[14] Finally, a metal electrode is deposited *via* thermal evaporator to complete the solar cell.

At present, tremendous attention has been paid on the optimization of this mesoporous TiO_2-based device, including the modification of the TiO_2 nanostructure, perovskite layer and HTM, along with the in-depth understanding on detailed mechanism behind this high efficiency device architecture.[73-77] So far, anatase TiO_2 nanoparticles are the most frequently and successfully used nanostructures to construct mesoscopic perovskite solar cell, with the highest PCE of over 17%. In 2014, Park and coworkers used rutile TiO_2 nanoparticles to fabricate a FTO/bl-TiO_2/mp-TiO_2(rutile)/$MAPbI_3$/**spiro-MeOTAD**/Au device.[78] Compared to the anatase TiO_2-based device, higher electron diffusion coefficients and lower electron recombination were observed in the rutile TiO_2-based device, suggesting that more electrons were injected from the perovskite to the rutile TiO_2 layer. As a result, although a relatively lower open-circuit voltage (*V*oc) was observed due to the lower Fermi energy level at equilibrium between TiO_2 and perovskite in the rutile-based device, optimal device demonstrated a PCE of 14.46%, with a short-circuit current density (*J*sc) of 20.02 mA cm^{-2}, a *V*oc of 1.022 V, and a fill factor (FF) of 0.71 at AM 1.5G one sun illumination.

Besides the mostly used TiO_2 nanoparticles, many other nanostructured TiO_2 materials, such as nanosheets,[14,79,80] nanorods,[81-85] nanotube,[86] nanofibers/nanowire[87-89] and single crystal,[90] were also tried to fabricate the mesoscopic TiO_2 structure, due to the reason that the physical and chemical properties of TiO_2 nanocrystals are affected not only by the intrinsic electronic structure, but also by their size, shape, organization, and surface properties. Jung and coworkers also fabricated a TiO_2 nanoparticle/ITO nanowire nanocomposite for use as a photoelectrode material.[91] However, compared with the state-of-the-art TiO_2 nanoparticle-based device, lower efficiencies were observed in these nanostructured TiO_2-based devices. Furthermore, researchers[70 82,85] also introduced a way of surface modification to improve the perovskite-based device performance by doping metal (e.g. Y, Mg, Nb) ion into the nanostructured TiO_2.

4.1.2 Device based on mesoporous *n*-type ZnO

Nanostructured ZnO is a viable *n*-type alternative scaffold to mesoporous TiO_2 for perovskite solar cells due to its comparable energy levels (band gap: ~3.37 eV at 25 °C) as well as relatively higher electron mobility.[92,93] The first example of such device was reported by Hagfeldt et al in 2013, in which the $MAPbI_3$ perovskite layer was one-step deposited on the top of vertically ordered ZnO nanorod arrays (NRAs) with **spiro-OMeTAD** as the HTM.[94] In this configuration, no dense TiO_2 layer was needed but replaced with a compact ZnO layer (bl-ZnO), which acted as not only a hole blocking layer but also a seed layer for the growth of the ZnO nanorods. ZnO NRAs were prepared by hydrothermal process, using equimolar zinc nitrate hexahydrate ($Zn(NO_3)_2 \cdot 6H_2O$) and hexamethylenetetramine (HMTA) as precursors. The diameter and length of ZnO nanorods could be controlled by changing the precursor concentration and growth time. A noteworthy feature is that although an increased nanorod length can result in a higher light harvesting efficiency due to the increased perovskite loading, an increased charge recombination could also come up, which will deteriorate the photovoltaic performance. Thus, it is necessary to seek a balance to achieve the optimal performance. Based on this ITO/bl-ZnO/NRA-ZnO (diameter/length =50 nm/1000 nm)/$MAPbI_3$/**spiro-OMeTAD**/Ag device, initial study yielded a PCE of 5%, with a *J*sc of 12.7 mA cm^{-2}, a *V*oc of 0.68 V, and a FF of 0.58 under 100 mW cm^{-2} AM 1.5 G illumination. [94] Later, by systematically controlling the diameter/length (82 nm/1000 nm) of ZnO NRAs and depositing the $MAPbI_3$ using SDP (see Figure 5), Park et al effectively increased the pore-filling of perovskite in ZnO NRAs film and further improved the PCE to 11.13%, with both increased *J*sc (20.08 mA cm^{-2}) and *V*oc (0.991 V). [95]

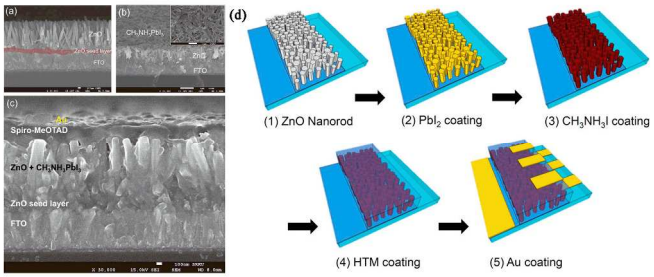

Fig. 5. SEM images of (a) bare ZnO nanorod grown on FTO substrate, (b) $MAPbI_3$-deposited ZnO nanorods, and (c) full cell. Inset in (b) is surface SEM image of the $MAPbI_3$ capping layer. (d) Fabrication procedure of perovskite solar cell（*via* SDP） based on the ZnO nanorod electrode. Reprinted with permission.[95]

Mathews and coworker also reported a ZnO NRAs-based all-low-temperature processed device, in which the ZnO nanorods were fabricated using chemical bath deposition (CBD) while the ZnO compact layer was formed by electrodeposition.[96] The typical ZnO nanorods diameters were in the range of 100–150 nm and the lengths were between 400–500 nm. Four type devices including FTO/bl-ZnO/$MAPbI_3$/HTM/Au (T_1), FTO/bl-ZnO/NRA-ZnO/$MAPbI_3$/HTM/Au (T_2), polyethylene terephthalate (PET)/FTO/bl-ZnO/$MAPbI_3$/HTM/Au (T_3), and PET/FTO/bl-ZnO/NRA-ZnO/$MAPbI_3$/HTM/Au (T_4), were fabricated and characterized. Relatively low PCEs were obtained in the condition without ZnO NRAs and at last, PCEs of 8.90% and 2.62% were achieved from the T_2 and T_4 devices, respectively.

In 2014, using plasma-enhanced chemical vapor deposition (PECVD), Ahmad et al prepared a nanocolumnar ZnO thin film on the compact TiO_2-coated FTO substrate at low temperature.[97] Under AM1.5G solar illumination (100 mW/cm^2), $MAPbI_3$-sensitized solar cell combined with **spiro-OMeTAD** or **PTAA** as the HTM yielded PCEs of 4.8% and 1.3%. Compared with the early result from Mathews et al[96], the FTO/bl-TiO_2/nanocolumns ZnO/$MAPbI_3$/**spiro-OMeTAD**/Au-based device demonstrated a similar *J*sc but significant decreased FF and *V*oc, which can be attributed to the higher charge recombination.

Recently , Mahmood and coworkers fabricated a mesoporous ZnO or Al-doped mesoporous ZnO (AZO) film using the electrospraying method and studied the performance of the result perovskite solar cells.[98] For the optimal device based on a pure ZnO film (~440 nm thick), a PCE of 10.8% was achieved, with a *J*sc of 16 mA cm^{-2}, a *V*oc of 1.01 V, and a FF of 0.67. When the ZnO film was doped with Al, device yielded a higher PCE of 12%, with obviously increased *V*oc (1.045 V) and FF (0.76). According to the reports,[99] doping of ZnO with metal can not only enhance its *n*-type characteristics (e.g. increasing the conductivity) but also help to shift the Fermi level in the direction of conduction band. As the *V*oc is mainly determined by the difference between the quasi-Fermi levels of the electrons in the *n*-type semiconductor and the holes in the HTM, thus, a lower electron recombination rate and higher electron concentration of the conduction band can be obtained, which is beneficial to enhance both the *V*oc and FF. Similar performance increase was also observed by Meng et al, by modifying the ZnO nanorod surface with a thin Al-doped ZnO layer, in a FTO/bl-ZnO/NRA-ZnO/AZO/$MAPbI_3$/HTM/Au-based device (*J*sc =19.77 mA cm^{-2}, *V*oc = 0.90 V, FF = 0.60 and PCE = 10.7%).[100]

Table 2. A summary of published representative results of mesoporous *n*-type ZnO-based MMOPSC performance parameters with different device fabrication methods and configurations

Perovskite Layer (PL)	DP	Device structure	*J*sc (mA/cm^2)	*V*oc (V)	FF (%)	PCE (%)	Ref.
$MAPbI_3$	OSPD	ITO/bl-ZnO/NRA-ZnO/PL/**spiro**/Ag	12.7	0.68	58	5.0	94
$MAPbI_3$	SDP	FTO/bl-ZnO/NRA-ZnO/PL/**spiro**/Au	20.08	0.991	56	11.13	95
$MAPbI_3$	SDP	FTO/bl-ZnO/PL/**spiro**/Au (T_1)	11.27	1.08	45.44	5.54	96
$MAPbI_3$	SDP	FTO/bl-ZnO/NRA-ZnO/PL/**spiro**/Au (T_2)	16.98	1.02	51.11	8.90	
$MAPbI_3$	SDP	PET/ITO/bl-ZnO/PL/**spiro**/Au (T_3)	5.57	0.99	39.58	2.18	
$MAPbI_3$	SDP	PET/ITO/bl-ZnO/NRA-ZnO/PL/**spiro**/Au (T_4)	7.52	0.80	43.14	2.62	
$MAPbI_3$	SDP	FTO/bl-TiO_2/nanocolumn ZnO/PL/**spiro**/Au	16	0.718	41.2	4.8	97
$MAPbI_3$	SDP	FTO/bl-TiO_2/nanocolumn ZnO/PL/**PTAA**/Au	8.3	0.481	32.7	1.3	
$MAPbI_3$	SDP	FTO/bl-ZnO/mp-ZnO/PL/**spiro**/Ag	16	1.01	67	10.8	98
$MAPbI_3$	SDP	FTO/bl-ZnO(Al)/mp-AZO/PL/**spiro**/Ag	15.1	1.045	76	12	
$MAPbI_3$	SDP	FTO/bl-ZnO/NRA-ZnO/AZO/PL/**spiro**/Au	19.77	0.90	60	10.7	100

4.1.3 Device based on mesoporous *p*-type NiO

Apart from devices based on mesoporous *n*-type metal oxide such as TiO_2 and ZnO, in 2014, Guo's group demonstrated a mesoscopic NiO/$MAPbI_3$/fullerene-derivative -based architecture using *p*-type NiO nanocrystalline as the selective contact (see Figure 6).[101] This inverted mesoporous configuration was initially developed from a planar perovskite solar cell with a flat electrode of oxide ITO/NiO_x (without the NiO nanocrystalline layer).[102,103] Compared with that planar devices with thin NiO films, the fabrication of mesoscopic NiO layer provided an increased film thickness to host the light absorbing perovskite material and prevented the risk of morphological defects that decreased the photovoltaic performance. The PCE of devices with ITO/bl-NiO_x/mp-NiO/$MAPbI_3$/[6,6]-phenyl C71-butyric acid methyl ester (**PC70BM**)/BCP/Al and ITO/bl-NiO_x/mp-NiO/$MAPbI_3$/**PC60BM**/BCP/Al structure reached to 9.44% and 9.51%, which are higher than that (7.4%) of the device based on ITO/bl-NiO_x/$MAPbI_3$/**PC60BM**/BCP/Al system. Later, using a low-temperature sputtered bl-NiO_x thin film instead of the solution-processed bl-NiO_x thin film, a higher PCE of 11.6% was achieved in this mp-NiO/$MAPbI_3$ heterojunction solar cell.[104]

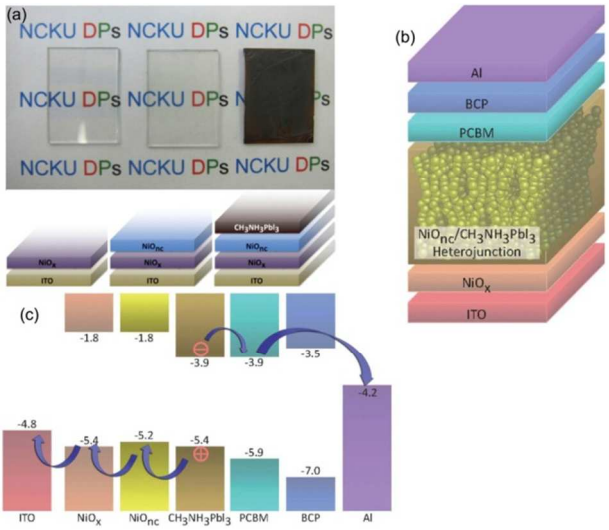

Fig. 6. (a) The photos and illustrations of patterned ITO glass, ITO glass with bl-NiO_x and mp- NiO with perovskite coated electrode. (b) The schematic of the whole device (ITO/bl-NiO_x/mp-NiO/$MAPbI_3$/**PC60BM** (or **PC70BM**)/BCP/Al). (c) The energy level diagram of the mp-NiO/perovskite/**PC60BM** heterojunction. Reprinted with permission.[101]

4.2 Meso-superstructured perovskite solar cells

In 2012, Snaith and coworkers put forward the concept of " meso-superstructured solar cell" for the first time.[13] In this case, a Cl mixed perovskite $MAPbI_{3-x}Cl_x$ was infiltrated within an insulating mp-Al_2O_3 film rather than the conventional mp-TiO_2 film. No photoexcited electrons were injected into Al_2O_3 but directly transport throughout the perovskite layer and were collected at the compact TiO_2-coated FTO electrode. (see Figure 7a) Unlike the mesoporous *n*-type TiO_2-based perovskite solar cells, the Al_2O_3 acts only as a "scaffold" and the perovskite layer functions both the intrinsic absorber and electron transporter. Faster electronic charge transportation in the perovskite layer was observed than that in the mesoporous TiO_2, and device based on mp-Al_2O_3 yielded a PCE of 10.9%, with a *J*sc of 17.8 mA cm^{-2}, a *V*oc of 0.98 V, and a FF of 0.63. It was found that a lower *V*oc (0.80 V) was measured for mp-TiO_2-based devices than that (0.98V) of mp-Al_2O_3-based device. Initial theories attributed this to the declined electron quasi-Fermi levels in TiO_2-based device, which resulted in a narrowed splitting of hole and electron quasi-Fermi levels. Since the *V*oc is directly related to the difference between the hole- and electron quasi-Fermi levels, this decreased electron quasi-Fermi levels will lead to a lower *V*oc in TiO_2-based device. Similar change of *V*oc was also reported by Hodes et al in $MAPbBr_3$ –based MSSCs using **PDI** as the HTM,[105] where device based on FTO/bl-TiO_2/mp-Al_2O_3/$MAPbBr_3$/**PDI**/Au structure yielded a *V*oc as high as 1.3V compared to the mp-TiO_2 based device with a *V*oc of 1 V.

In 2013, using a thin Al_2O_3 film (~80 nm) processed in low temperature (<150℃), Snaith et al fabricated a "flat-junction" thin film solar cell with a thick perovskite "capping layer" on the top of the scaffold (see Figure 7b), and improved the FTO/bl-TiO_2/mp-Al_2O_3/$MAPbI_{3-x}Cl_x$/**spiro-OMeTAD**/Ag-based device efficiency to 12.3% (*J*sc =18 mA cm^{-2}, *V*oc = 1.02 V, and FF = 0.67).[67] Later, by incorporating core−shell Au@SiO_2 nanoparticles (np-Au@SiO2) into the porous Al_2O_3 scaffold, the authors achieved significantly enhanced *J*sc and PCE in the "Au@SiO_2" device (*J*sc = 16.91 mA cm^{-2}, PCE = 11.4%) compared to the "Al_2O_3-only" device (*J*sc =14.76 mA cm^{-2}, PCE = 10.7%), and introduced a new enhancement mechanism of reduced exciton binding energy with the incorporation of the metal nanoparticles, rather than enhanced light absorption.[106] Worsley and coworkers reported a simplified one-step deposition process for Al_2O_3-perovskite layer: A mixed DMF solution containing Al_2O_3 nanoparticles (np-Al_2O_3) and the $MAPbI_{3-x}Cl_x$ perovskite precursor was directly spin-coated on the compact TiO_2 layer, followed by a thermal treatment at low temperature (<110 °C).[107] Device based on this co-deposited Al_2O_3–perovskite film, in which 5 wt% alumina in the precursor solution prior to spin-coating, yielded a highest PCE of 7.16%, with a *J*sc of 12.78 mA cm^{-2}, a *V*oc of 0.925 V, and a FF of 0.61. In 2014, Snaith and coworkers introduced a method to passivate the hole trapping states at the perovskite ($MAPbI_{3-x}Cl_x$) surface by assembling iodopentafluorobenzene (IPFB) *via* supramolecular halogen bonding.[108] The passivation of the undercoordinated halides effectively reduced the density of accumulated charge at the perovskite/HTM heterojunction, leading to an increased FF (0.67) compared to that (0.57) in unpassivated device and a high PCE of 15.7%. Later, using a low Al-doping TiO_2 blocking layer (0.3 mol%), the authors also observed an increased *J*sc (20 mA cm^{-2}) and PCE (13.8%) compared with the undoped device (*J*sc = 16.04 mA cm^{-2}, PCE = 11.13%) due to the improved conductivity of Al-doping TiO_2.[109] Recently, by replacing the organic HTM with **P3HT**-functionalized single-walled carbon nanotubes (SWNTs) embedded in an insulating poly(methyl methacrylate) (PMMA) matrix, MSSC device with unprecedented resilience against thermal stressing and moisture ingress was fabricated, and yielded a PCE of 15.3% with an average efficiency of 10±2%.[110]

In spite of the elimination of high temperature sintering steps for the mesoporous Al_2O_3 scaffold, a high sintering temperature is still needed for the compact TiO_2 layer (~500 °C) in MSSCs, which lacks the compatibility with flexible substrates and thus presents a drawback in view of large scale industrial manufacture. In the end of 2013, by spin-coating the nanocomposites of graphene nanoflakes/TiO_2 nanoparticles on the top of FTO-coated substrates, Snaith and coworkers fabricated a low temperature processed electron collection layers at 150 °C.[111] The superior charge mobility and proper work function of graphene effectively improved the electrical conductivity and reduced the formation of energy barriers at the material interfaces, leading to an excellent device efficiency of 15.6%. Subsequently, the authors reported a new route for fabricating a low temperature processed TiO_2 compact layer (<150 °C). Compared with the previous MSSCs based on a high temperature sintered compact TiO_2 layer, this all-low-temperature processed device yielded a PCE of up to 15.9%, with a *J*sc of 21.5 mA cm^{-2}, a *V*oc of 1.02 V, and a FF of 0.71 under simulated AM1.5 100 mW cm^{-2} sunlight. Also, the PCE of 15.9% is the highest reported value for Al_2O_3-based MSSCs.[22] Furthermore, Yuan and coworker also reported the use of compact ZnO layers which fabricated by ALD at 70 °C, and achieved PCEs of 13.1% under standard AM1.5 illumination.[112]

Besides the Al_2O_3-based MSSCs, in 2013, Johansson[46] and Park[113] et al reported another type MSSC based on nanostructed ZrO_2 scaffold, Like Al_2O_3, the much higher conduction band of ZrO_2 than that of perovskite blocks the electron injection with no charge separation at the ZrO_2/perovskite interface. Finally, using a SDP method, a PCE of 10.8% was achieved from this mp-ZrO_2/$MAPbI_3$-based device, with a high *V*oc up to 1.07 V. In 2014, Jiang and coworkers also fabricated a scaffold layer composed of SiO_2 nanoparticles for perovskite solar cells.[114] By controlling the size of the SiO_2 nanoparticles, optimal FTO/bl-TiO_2/mp-SiO_2/$MAPbI_{3-x}Cl_x$/**spiro-OMeTAD**/Au-based devices yielded a PCE of 11.45%, with a *J*sc of 16.4 mA cm^{-2}, a *V*oc of 1.05 V, and a FF of 0.66.

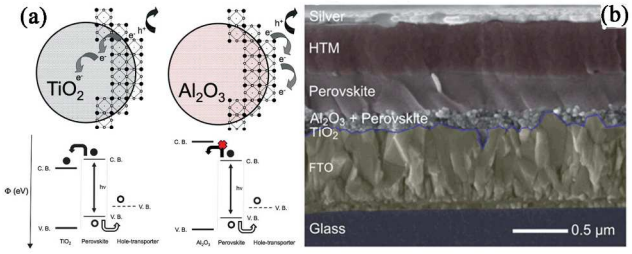

Fig. 7. (a) The schematic of perovskite-coated TiO_2 and Al_2O_3, illustrating electron and hole transfer. Reprinted with permission.[13] (b) The schematic of MSSC with a thin Al_2O_3 layer. Reprinted with permission.[67]

Table 3. A summary of published representative results of MSSC performance parameters with different device fabrication methods and configurations

PL	DP	Device structure	*J*sc (mA/cm^2)	*V*oc (V)	FF (%)	PCE (%)	Ref.
$MAPbI_{3-x}Cl_x$	OSPD	FTO/bl-TiO_2/mp-Al_2O_3/PL/**spiro**/Ag	17.8	0.98	63	10.9	13
$MAPbI_{3-x}Cl_x$	OSPD	FTO/bl-TiO_2/mp-Al_2O_3/PL/**spiro**/Ag	18	1.02	67	12.3	67
$MAPbI_{3-x}Cl_x$	OSPD	FTO/bl-TiO_2/mp-Al_2O_3(np-Au@SiO_2)/PL/**spiro**/Ag	16.91	1.02	64	11.4	106
$MAPbI_{3-x}Cl_x$	OSPD	FTO/bl-TiO_2/PL(np-Al_2O_3)/**spiro**/Au	12.78	0.925	61	7.16	107
$MAPbI_{3-x}Cl_x$	OSPD	FTO/bl-TiO_2/mp-Al_2O_3/PL/IPFB/**spiro**/Ag	23.38	1.06	67	15.7	108
$MAPbI_{3-x}Cl_x$	OSPD	FTO/bl-TiO_2(Al)/mp-Al_2O_3/PL/**spiro**/Ag	20	1.07	65	13.8	109
$MAPbI_{3-x}Cl_x$	OSPD	FTO/bl-TiO_2/mp-Al_2O_3/PL/**P3HT**-SWNTs-PMMA/Ag	22.71	1.02	66	15.3	110
$MAPbI_{3-x}Cl_x$	OSPD	FTO/bl-TiO_2(grapheme)/mp-Al_2O_3/PL/**spiro**/Au	21.9	1.04	73	15.6	111
$MAPbI_{3-x}Cl_x$	OSPD	FTO/bl-TiO_2/mp-Al_2O_3/PL/**spiro**/Ag	21.5	1.02	71	15.9	22
$MAPbI_3$	OSPD	FTO/bl-ZnO/mp-Al_2O_3/PL/**spiro**/Ag	20.4	0.976	66	13.1	112
$MAPbI_3$	SDP	FTO/bl-TiO_2/mp-ZrO_2/PL/**spiro**/Ag	17.3	1.07	59	10.8	46
$MAPbI_{3-x}Cl_x$	OSPD	FTO/bl-TiO_2/mp-SiO_2/PL/**spiro**/Au	16.4	1.05	66	11.45	114

4.3 Planar heterojunction perovskite solar cells

During the initial studies on MSSCs with Al_2O_3 scaffold, Snaith and coworkers also fabricated a planar heterojunction perovskite solar cell based on a simple FTO/bl-TiO_2/$MAPbI_{3-x}Cl_x$/**spiro-OMeTAD**/Ag structure. No porous metal-oxide structure was needed in this configuration and perovskite actually functioned as the ambipolar layer in a *p*-i-*n* junction, where the intrinsic (i) layer is the perovskite absorber. Preliminary research findings yielded PCEs from 1.8%[13] to 4.9%[67], and nearly 100% internal quantum efficiency (IQE) was measured.[67] Also, it has been discovered that the typical 3-D organolead trihalide perovskites exhibit large charge carrier diffusion lengths (~100 nm for triiodide perovskite and >1μm for the mixed halide perovskite with Cl). [115,116] All above mentioned indicate the possibility of this planar configuration to be a high efficient architecture. In fact, A PHJ structure can not only simplify the device fabrication process but also avoid the pore filling problem in the mesosuperstuctured device, which always leads to a large standard deviation. At present, two configurations for this planar device including a positive or inverted structure have been reported, in which a *n*-type (e.g. TiO_2, ZnO) or *p*-type conductor (e.g. PETDOT:PSS, NiO, CuSCN, graphene oxide, polythiophene) was coated on a conductive glass, and both yielded excellent PCEs.

4.3.1 Device based on a positive configuration

For this originally emerged PHJ perovskite solar cell (bl-TiO_2/perovskite/**spiro-OMeTAD**), the morphology of absorber layer is the critical factor in determining the resulting device performance. In 2013, through carefully varying the processing conditions, such as the annealing temperature and perovskite film thickness, compact TiO_2 layers with a high $MAPbI_{3-x}Cl_x$ perovskite (*via* OSPD) coverage were obtained by Snaith et al, and a breakthrough PCE of 11.4% was achieved under standard AM1.5G illumination, with a *J*sc of 20.3 mA cm^{-2}, a *V*oc of 0.89 V, a FF of 0.64.[31] Later, using DSVD or SDP, Snaith[19] and Bein[43,117] et al further improved the bl-TiO_2/$MAPbI_{3-x}Cl_x$/**spiro-OMeTAD**-based device effieicncy to ~15%. Yang and coworkers also formed high-quality planar $MAPbI_3$ films by VASP and achieved a PCE of 12.1% (bl-TiO_2/$MAPbI_3$/**spiro-OMeTAD**).[48] Yella et al introduced a low-temperature route for the fabrication of FTO/bl-TiO_2(rutile)/$MAPbI_3$/**spiro-OMeTAD**/Au solar cell and obtained a higher PCE (13.7%) compared to the device with compact TiO_2 (anatase) layer (3.7%).[66] A noteworthy feature was that a relatively lower *J*sc (< 20 mA cm^{-2}) was observed for pure iodide-based perovskite solae cells, which could be attributed to the shorter electron–hole diffusion lengths (on the order of 100 nm) than that of Cl-mixed perovskite.[115,116] Han and coworkers recently optimized the SDP using a strongly coordinative solvent of DMSO instead of the commonly used DMF to dissolve PbI_2 and fabricate PbI_2 films, and achieved a high converted $MAPbI_3$ perovskite film with relatively uniform distributions of crystal sizes.[41] PHJ devices demonstrated good reproducibility and yielded the highest PCE of 13.5% (*J*sc =20.71 mA cm^{-2}, *V*oc = 1.02 V, and FF = 0.64), with an average efficiency of 12.5%. Spiccia and coworkers also reported a one-step, solvent-induced, fast crystallization method to control the dynamics of nucleation and grain growth of $MAPbI_3$.[27] Device based on FTO/bl-TiO_2/$MAPbI_3$/**spiro-OMeTAD**/Ag structure yielded the maximum PCE of 16.2% under standard AM 1.5 condition (*J*sc =21.1 mA cm^{-2}, *V*oc = 1.04 V, and FF = 0.74).

In 2013, Kelly and coworkers reported the use of a thin ZnO nanoparticles film (~25nm) as an electron-transport layer in an ITO/bl-ZnO/$MAPbI_3$/**spiro-OMeTAD**/Ag structure PHJ solar cell.[47] Higher electron mobility of ZnO compared to TiO_2[92] and large crystallite size on the surface of the ITO/bl-ZnO/$MAPbI_3$ layer resulted in a higher *J*sc (20.4 mA cm^{-2}) with a PCE of 15.7%. Considering that no sintering or annealing step is required for fabricating ZnO layer, the device on a flexible ITO/PET substrate was prepared, yielding a *V*oc of 1.03 V, a *J*sc of 13.4 mA cm^{-2}, a FF of 0.739 and a PCE of 10.2%. Also, the PCE of 10.2% was the highest value in the reported flexible perovskite devices. Later, Lee et al used a simple **PC60BM** modified, sol-gel processed ZnO layer, as the electron conductor.[118] Through this interfacial engineering, higher *V*oc values were observed in devices with bl-ZnO/**PC60BM** substrates compared to that of devices with only ZnO, and a PCE of 12.2% was achieved in ITO/bl-ZnO/**PC60BM**/$MAPbI_3$/**sprio-OMeTAD**/MoO_3/Ag-based devices. Bai and coworkers also reported low-temperature magnetron sputtered ZnO nanorods film as the cathode interlayer for ITO/bl-ZnO/$MAPbI_3$/**sprio-OMeTAD**/MoO_3/Ag-based device and achieved PCEs of 13.4% and 8.03% respectively in glass/ITO- and PET/ITO-based substrates.[119]

Besides the above-mentioned TiO_2 or ZnO-based positive devices using **sprio-OMeTAD** as the HTM, other type *p*-i-*n*

junctions with different *p*-type HTMs such as organic **P3HT**[63,64], **PTB7-Th**[118], **DR3TBDTT**[120] and inorganic CuSCN[121] were also reported, with favorable performance achieved.

Very recently, through a method of Lewis base passivation,[122] which the crystal surfaces were treated with the Lewis bases thiophene and pyridine, a significant decrease in the rate of nonradiative recombination in perovskite films was measured by Snaith et al. The authors thought that the under-coordinated Pb ions in the perovskite crystal could be bound with Lewis base molecules, thus passivating these defect sites. At last, PCEs of 15.3% and 16.5% were achieved using thiophene and pyridine treated $MAPbI_{3-x}Cl_x$ respectively in FTO/bl-TiO_2/$MAPbI_{3-x}Cl_x$/Lewis base/**spiro-OMeTAD**/Au-based device. Yang's group fabricated a modified planar configuration with an ITO/PEIE/bl-TiO_2(Y)/$MAPbI_{3-x}Cl_x$/**spiro-OMeTAD**/Au structure, in which ITO was coated with polyethyleneimine ethoxylated (PEIE) while TiO_2 was doped with yttrium (Y) (see Figure 8).[23] The PEIE – modified ITO effectively reduces the work function of ITO from 4.6 eV to 4.0 eV, which is beneficial to the efficient electron transport between the TiO_2 and ITO layers. Also, like the Al-doped ZnO mentioned above,[98] the doping of TiO_2 with Y not only improves the conductivity (from 6×10^{-6} S/cm to 2×10^{-5} S/cm) but also raises the Fermi level in the Y-TiO_2 layer. At last, this all-low-temperature processed device yielded a record PCE of 19.3% with an average PCE of 16.6%.

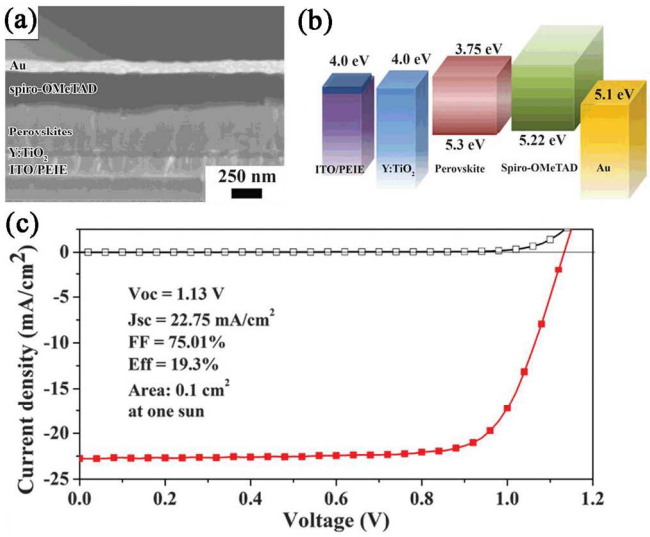

Fig. 8. (a) SEM cross-sectional image of the device. (b) Diagram of energy levels (relative to the vacuum level) of each functional layer in the device. (c) *J-V* curves for the champion cell without antireflective coating. Reprinted with permission.[23]

Table 4. A summary of published representative results of positive PHJPSC performance parameters with different device fabrication methods and configurations

PL	PL thickness (nm)	DP	Device structure	*J*sc (mA/cm^2)	*V*oc (V)	FF (%)	PCE (%)	Ref.
$MAPbI_{3-x}Cl_x$	400-800	OSPD	FTO/bl-TiO_2/PL/**spiro**/Au	20.3	0.89	64	11.4	31
$MAPbI_{3-x}Cl_x$	~330	DSVD	FTO/bl-TiO_2/PL/**spiro**/Ag	21.5	1.07	67	15.4	19
$MAPbI_{3-x}Cl_x$	~400	SDP	FTO/bl-TiO_2/PL/**spiro**/Au	22.9	0.98	69	14.82	43,117
$MAPbI_3$	~350	VASP	FTO/bl-TiO_2/PL/**spiro**/Ag	19.8	0.924	66.3	12.1	48
$MAPbI_3$	~300	SDP	FTO/bl-TiO_2(rutile)/PL/**spiro**/Au	19.8	1.05	64	13.7	66
$MAPbI_3$	~300	SDP	FTO/bl-TiO_2/PL/**spiro**/Au	20.71	1.02	64	13.5	41
$MAPbI_3$	~350	OSPD	FTO/bl-TiO_2/PL/**spiro**/Ag	21.1	1.04	74	16.2	27
$MAPbI_3$	~300	SDP	ITO/bl-ZnO/PL/**spiro**/Ag	20.4	1.03	74.9	15.7	47
$MAPbI_3$	~300	SDP	PET/ITO/bl-ZnO/PL/**spiro**/Ag	13.4	1.03	73.9	10.2	
$MAPbI_3$	NA	SDP	ITO/bl-ZnO/**PC60BM**/PL/**sprio**/MoO_3/Ag	18.18	1.00	67	12.2	118
$MAPbI_3$	NA	SDP	ITO/bl-ZnO/PL/**sprio**/MoO_3/Ag	22.4	1.04	57.4	13.4	119
$MAPbI_3$	NA	SDP	PET/ITO/bl-ZnO/PL/**sprio**/MoO_3/Ag	18.4	0.87	49.7	8.03	
$MAPbI_{3-x}Cl_x$	NA	OSPD	ITO/bl-TiO_2/PL/**P3HT**/Ag	21	0.936	69.1	13.6	63,64
$MAPbI_3$	NA	SDP	ITO/bl-ZnO/**PC60BM**/PL/**PTB7-Th**/MoO_3/Ag	15.1	1,03	71	11.04	118
$MAPbI_{3-x}Cl_x$	~350	SDP	FTO/bl-TiO_2/PL/**DR3TBDTT**/Au	15.3	0.95	60	8.8	120
$MAPbI_3$	~400	OSPD	FTO/bl-TiO_2/PL/CuSCN/Au	14.4	0.727	61.7	6.4	121
$MAPbI_{3-x}Cl_x$	NA	OSPD	FTO/bl-TiO_2/$MAPbI_{3-x}Cl_x$/thiophene/**spiro**/Au	21.3	1.02	68	15.3	122
$MAPbI_{3-x}Cl_x$	NA	OSPD	FTO/bl-TiO_2/$MAPbI_{3-x}Cl_x$/pyridine/**spiro**/Au	24.1	1.05	72	16.5	
$MAPbI_{3-x}Cl_x$	~350	OSPD	ITO/PEIE/bl-TiO_2(Y)/PL/**spiro**/Au	22.75	1.13	75.01	19.3	23

4.3.2 Device based on an inverted configuration

In 2013, inspired by the structure of bulk-heterojunction (BHJ) organic solar cells, Guo and coworkers firstly reported a series of bilayer inverted devices based on a PHJ of $MAPbI_3$ perovskite/fullerene-derivative structure, in which $MAPbI_3$ acted as a "donor" material while **C60**, **PC60BM** or indene-C_{60} bisadduct **(IC60BA)** as the "acceptor" material (consisting of Glass/ITO/PEDOT:PSS as the positive electrode, a thin bathocuproine (BCP) film as the hole-blocking layer, and an Al negative electrode).[123] Under standard 1 sun AM 1.5 simulated solar irradiation (100 mW cm^{-2}), *V*oc was varied with the LUMO levels of acceptors, proving the formation of a donor–acceptor interface. Different solvents (GBL or DMF) were used

to control the $MAPbI_3$ perovskite thin film morphologies and optimal devices containing $MAPbI_3$/**C60**, $MAPbI_3$/**PC60BM** or $MAPbI_3$/**IC60BA** showed PCE of 3.0%, 3.9% or 3.4%, respectively. Subsequently, Lam et al reported a similar system with a ITO/PEDOT:PSS/$MAPbI_3$/**PC60BM**/Al structure.[124] High photovoltaic performance and an IQE of close to 100% were observed, suggesting the highly efficient exciton diffusion, charge transfer and charge collection. Devices fabricated with OSPD method yielded a *J*sc of 8.2 mA cm^{-2}, a *V*oc of 0.82 V, a FF of 0.77 and a PCE of 5.2% while a PCE of 7.4% was obtained using SDP, with a *J*sc of 10.8 mA cm^{-2}, a *V*oc of 0.91 V, and a FF of 0.76 under AM 1.5G illumination (100 mW cm^{-2}).

Around the same time, Snaith, Bolink, and Yang reported independently several perovskite PHJ solar cells with high PCEs up to or over 10%. Snaith et al demonstrated a device structure consisting of FTO/PEDOT:PSS/$MAPbI_{3-x}Cl_x$/**PC60BM**/TiO_x/Al in which a bilayer of **PC60BM** and compact-TiO_x were employed as the *n*-type charge collection layer.[125] A PCE of 9.8% was obtained, with a *J*sc of 15.8 mA cm^{-2}, a *V*oc of 0.94 V, and a FF of 0.66. Also, a PCE of 6.4% was achieved for the same configuration on an ITO-coated PET plastic foil. Interestingly, when fabricating devices on ITO-covered glass, an obvious decrease of *J*sc and FF were observed which is likely arise from poorer perovskite film formation and lower surface coverage upon the PEDOT:PSS-coated ITO as opposed to the PEDOT:PSS-coated FTO. Bolink et al reported a $MAPbI_3$ perovskite solar cell in which a highly oriented pure $MAPbI_3$ film was sandwiched between an electron-blocking **Poly-TPD** layer and a hole-blocking **PC60BM** layer (ITO/PEDOT:PSS/**Poly-TPD**/$MAPbI_3$/**PC60BM**/Au).[126] High *J*sc of 16.12 mA cm^{-2} and the *V*oc of 1.05 V revealed that very few electrons and holes recombine and at last, a PCE of 12.04% (cell area = 0.09 cm^2) was achieved at the standard solar AM1.5G intensity of 100 mW cm^{-2}（the PCE was further improved to 14.8% with a 0.065 cm^2 solar cell[127]）. Yang and coworkers also fabricated two PHJ devices based on ITO/PEDOT:PSS/$MAPbI_{3-x}Cl_x$/**PC60BM**/Al and ITO/PEDOT:PSS/$MAPbI_{3-x}Cl_x$/ZnO/Al, yielding PCEs of 11.5% and 10.53% in rigid substrate, respectively (a 9.2% efficiency was achieved in PET/ITO/PEDOT:PSS/$MAPbI_{3-x}Cl_x$/**PC60BM**/Al-based flexible devices).[128] Later, Jen et al reported a simple way to enhance the crystallization of solution-processed perovskite by incorporating additives into its precursor solution to modulate thin film formation.[35] The device derived from the 1% DIO solution (FTO/PEDOT:PSS/$MAPbI_{3-x}Cl_x$/**PC60BM**/**Bis-C60**/Ag) exhibited a PCE of 11.8%, with a *J*sc of 17.5 mA cm^{-2}, a *V*oc of 0.92 V, and a FF of 0.73, compared to the 9.0% PCE of the device without using DIO. Similar enhancement was observed in the case on ITO substrates. Also, the relatively lower performance of ITO-based device than FTO-based device was consistent with Snaith's experiment. Lee et al used a new self-organized hole extraction layer, which was composed of PEDOT:PSS and a perfluorinated ionomer (PFI) to modified the interface work function and then reduce the potential energy loss.[129] Device based on a ITO/PEDOT:PSS/PFI/$MAPbI_3$/**PC60BM**/Al structure yielded an enhanced performance (PCE = 11.7%, *J*sc = 16.7 mA cm^{-2}, *V*oc = 0.982 V, FF = 0.705) compared to that of ITO/PEDOT:PSS/$MAPbI_3$/**PC60BM**/Al-based device (PCE = 8.1%, *J*sc = 14.1 mA cm^{-2}, *V*oc = 0.835 V, FF = 0.685). Also, a 8.0% efficiency was achieved in flexible perovskite solar cells with this self-organized hole extraction layer on a PET/ITO substrate. Seok and coworkers also used a solvent-engineering technology, which employed a mixture solution of DMSO : GBL (3 : 7, v/v), to fabricate the uniform and dense perovskite layer, and further improved the PCE to 14.1% in ITO/PEDOT:PSS/$MAPbI_3$/**PC60BM**/LiF/Al-based devices.[26]

Huang and coworkers fabricated two type PHJ perovskite solar cells with a ITO/PEDOT:PSS/$MAPbI_3$/**PC60BM**/**C60**/BCP/Al or ITO/PEDOT:PSS/$MAPbI_3$/**IC60BA**/**C60**/BCP/Al structure (see Figure 9).[130] A unique double fullerene layer was adopted in these devices which could effectively reduce dark current leakage by forming a Schottky junction with the anode. Though varying the ratio and concentration of the precursor solutions, the morphology, absorption and crystallization of perovskite films could be tuned and at last, optimal device with an **IC60BA** acceptor layer exhibited a best PCE of 12.2%, with a *J*sc of 15.7 mA cm^{-2}, a *V*oc of 0.97 V, and a FF of 0.80. Later, using a new film forming method by interdiffusion of spin-coated stacking layers of PbI_2 and MAI (*via* TSSD), a high quality film was achieved by Huang et al.[49] Perovskite based on a ITO/PEDOT:PSS/$MAPbI_3$/**PC60BM**/**C60**/BCP/Al system gave a PCE of 15.3%, with a relatively high *J*sc of 20.59 mA cm^{-2} under AM 1.5 simulated one sun illumination (further optimization using solvent annealing achieved a PCE of 15.6% with a perovskite thickness of 630 nm[131]) . Recently, Lin[56] and Wu[50] also obtained high PCEs of 15.4% and 16.3% in ITO/PEDOT:PSS/$MAPbI_{3-x}Cl_x$/**C60**/Bphen/Ca/Ag-based and ITO/PEDOT:PSS/$MAPbI_3$/**PC70BM**/Ca/Al-based devices using SVD or TSSD.

Apart from the most widely used PEDOT:PSS, in early 2014, Guo and coworkers replaced the PEDOT:PSS layer with a thin NiO_x interlayer (~10nm).[102] Device containing ITO/NiO_x/$MAPbI_3$/**C60**/BCP/Al and ITO/NiO_x/$MAPbI_3$/**PC60BM**/BCP/Al showed PCEs of 5.7% and 7.8% respectively with enhanced *V*oc compared to devices using PEDOT:PSS layer. The authors attributed this to the less energy loss for hole in NiO_x/$MAPbI_3$ junction and a better surface coverage of $MAPbI_3$ film on the glass/ITO/NiO_x substrate. Sarkar and coworkers also reported two type $MAPbI_{3-x}Cl_x$ perovskite solar cells with a FTO/NiO/$MAPbI_{3-x}Cl_x$/**PC60BM**/Ag or FTO/CuSCN/$MAPbI_{3-x}Cl_x$/**PC60BM**/Ag structure.[132] Devices with this electrodeposited NiO film and CuSCN film exhibited a PCE of 7.26% and 3.8%, respectively. Later, Yang et al used a sol–gel process to fabricate a thin NiO nanocrystalline film (~40 nm) for the development of a FTO/NiO/$MAPbI_3$/**PC60BM**/Au-based solar cell, and further improved the PCE to 9.11%.[133] Recently, by using a thin graphene oxide (**GO**) (~2 nm) [134] or polythiophene (**PT**) (~18 nm)[135] layer as a new *p*-type conductor instead of PEDOT:PSS, PCEs of 12.4% and 11.8% were achieved in ITO/**GO**/$MAPbI_{3-x}Cl_x$/**PC60BM**/ZnO/Al and ITO/**PT**/$MAPbI_3$/**C60**/BCP/Ag-based devices, respectively.

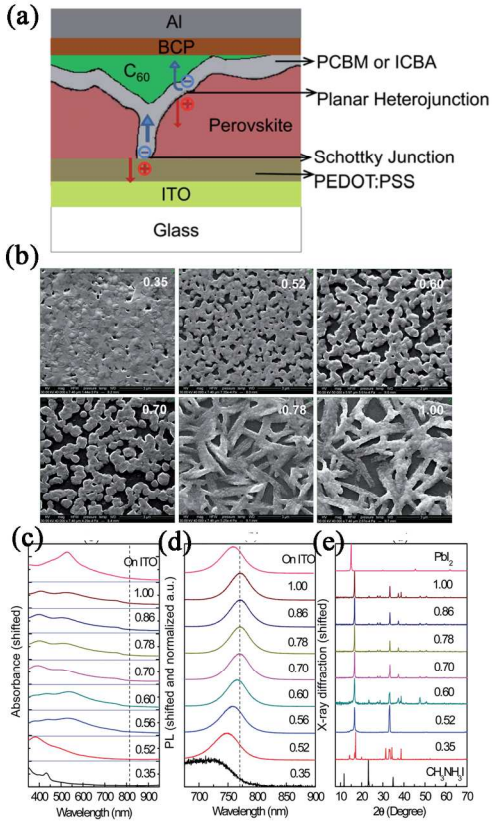

Fig. 9. (a) The schematic device structure. (b) Top view SEM images. (c) Absorption spectra. (d) photoluminescence spectra and (e) XRD patterns of the iodine perovskite films spun from solutions with a precursor ratio from 0.35 to 1. Reprinted with permission.[130]

Table 5. A summary of published representative results of invert PHJPSC performance parameters with different device fabrication methods and configurations

PL	PL thickness (nm)	DP	Device structure	*J*sc (mA/cm^2)	*V*oc (V)	FF (%)	PCE (%)	Ref.
$MAPbI_3$	20~30	OSPD	ITO/PEDOT:PSS/PL/**C60**/BCP/Al	9.02	0.55	61	3.0	123
$MAPbI_3$	20~30	OSPD	ITO/PEDOT:PSS/PL/**PC60BM**/BCP/Al	10.32	0.60	63	3.9	
$MAPbI_3$	20~30	OSPD	ITO/PEDOT:PSS/PL/**IC60BA**/BCP/Al	10.03	0.58	58	3.4	
$MAPbI_3$	50±5	OSPD	ITO/PEDOT:PSS/PL/**PC60BM**/Al	8.2	0.82	77	5.2	124
$MAPbI_3$	110±5	SDP	ITO/PEDOT:PSS/PL/**PC60BM**/Al	10.8	0.91	76	7.4	
$MAPbI_{3-x}Cl_x$	300~400	OSPD	FTO/PEDOT:PSS/PL/**PC60BM**/TiO_x/Al	15.8	0.94	66	9.8	125
$MAPbI_{3-x}Cl_x$	300~400	OSPD	ITO/PEDOT:PSS/PL/**PC60BM**/TiO_x/Al	14.4	0.92	47	6.3	
$MAPbI_{3-x}Cl_x$	300~400	OSPD	PET/ITO/PEDOT:PSS/PL/**PC60BM**/TiO_x/Al	14.4	0.88	51	6.4	
$MAPbI_3$	~285	DSVD	ITO/PEDOT:PSS/**Poly-TPD**/PL/**PC60BM**/Au	16.12	1.05	67	12.04	126
$MAPbI_{3-x}Cl_x$	~340	OSPD	ITO/PEDOT:PSS/PL/**PC60BM**/Al	18.5	0.87	72	11.5	128
$MAPbI_{3-x}Cl_x$	~340	OSPD	ITO/PEDOT:PSS/PL/ZnO/Al	17.29	0.886	68.76	10.53	
$MAPbI_{3-x}Cl_x$	~340	OSPD	PET/ITO/PEDOT:PSS/PL/**PC60BM**/Al	16.5	0.86	64	9.2	
$MAPbI_{3-x}Cl_x$	~400	OSPD	ITO/PEDOT:PSS/PL/**PC60BM**/**Bis-C60**/Ag	15	0.90	58	7.9	35
[a]$MAPbI_{3-x}Cl_x$	~400	OSPD	ITO/PEDOT:PSS/PL/**PC60BM**/**Bis-C60**/Ag	15.6	0.92	71	10.3	
$MAPbI_{3-x}Cl_x$	~400	OSPD	FTO/PEDOT:PSS/PL/**PC60BM**/**Bis-C60**/Ag	16	0.90	62	9	
[a]$MAPbI_{3-x}Cl_x$	~400	OSPD	FTO/PEDOT:PSS/PL/**PC60BM**/**Bis-C60**/Ag	17.5	0.92	73	11.8	
$MAPbI_3$	NA	TSSD	ITO/PEDOT:PSS/PFI/PL/**PC60BM**/Al	16.7	0.982	70.5	11.7	129
$MAPbI_3$	NA	TSSD	PET/ITO/PEDOT:PSS/PFI/PL/**PC60BM**/Al	15.5	1.04	49.9	8.0	
$MAPbI_3$	~290	OSPD	ITO/PEDOT:PSS/PL/**PC60BM**/LiF/Al	20.7	0.886	78.3	14.1	26

$MAPbI_3$	~140	OSPD	ITO/PEDOT:PSS/PL/**PC60BM**/**C60**/BCP/Al	15.9	0.88	72.2	10.1	130
$MAPbI_3$	~140	OSPD	ITO/PEDOT:PSS/PL/**IC60BA**/**C60**/BCP/Al	15.7	0.97	80.1	12.2	
$MAPbI_3$	270-300	TSSD	ITO/PEDOT:PSS/PL/**PC60BM**/**C60**/BCP/Al	19.6	0.99	79.3	15.4	49
$MAPbI_3$	~630	TSSD	ITO/PEDOT:PSS/PL/**PC60BM**/**C60**/BCP/Al	21.0± 0.5	0.96± 0.02	76.0± 1.5	15.6	131
$MAPbI_{3-x}Cl_x$	~430	SVD	ITO/PEDOT:PSS/PL/**C60**/Bphen/Ca/Ag	20.9	1.02	72.2	15.4	56
$MAPbI_3$	~360	TSSD	ITO/PEDOT:PSS/PL/**PC70BM**/Ca/Al	19.98	1.05	78	16.31	50
$MAPbI_3$	~60	OSPD	ITO/NiO_x/PL/**C60**/BCP/Al	12.95	0.74	60	5.7	102
$MAPbI_3$	~60	OSPD	ITO/NiO_x/PL/**PC60BM**/BCP/Al	12.43	0.92	68	7.8	
$MAPbI_{3-x}Cl_x$	NA	DSVD	FTO/NiO/PL/**PC60BM**/Ag	14.2	0.786	65	7.26	132
$MAPbI_{3-x}Cl_x$	NA	DSVD	FTO/CuSCN/PL/**PC60BM**/Ag	NA	NA	NA	3.8	
$MAPbI_3$	~250	SDP	FTO/NiO/PL/**PC60BM**/Au	16.27	0.882	63.5	9.11	133
$MAPbI_{3-x}Cl_x$	~170	OSPD	ITO/**GO**/PL/**PC60BM**/ZnO/Al	17.46	1.00	71	12.40	134
$MAPbI_3$	250±20	SDP	ITO/**PT**/PL/**C60**/BCP/Ag	16.2	1.03	70.7	11.8	135

[a] with 1%DIO

5. Hole-transporting materials (HTMs) for perovskite solar cells

Despite the rapid increase in efficiency associated with the evolution of different types of perovskites and device fabrication techniques, the development of HTM is very limited and mainly focused on organic compounds. In particular, the bulky 3-D **spiro-OMeTAD** (see Figure 10) with the twisted spirobifluorene center, has been proven as the most potential hole conductor for state-of-the-art perovskite-based devices since it was firstly introduced in 1998 for ss-DSSCs.[10] So far, based on **spiro-OMeTAD** HTM, MMOPSCs,[21] MSSCs[22] and PHJPSCs[23] have repectively showed their best device performance. However, the tedious synthesis of **spiro-OMeTAD** represents a potential hurdle to the future commercialization due to its high cost. So looking for new kinds of alternative HTMs to **spiro-OMeTAD** with sampler synthetic route, lower production cost and comparable device performance is very necessary. Also, a compatible HOMO energy level relative to perovskites and high charge-carrier mobility should also be considered. In the past two years, many new-type HTMs including, organic small molecules, polymers and inorganic materials, have been used for perovskite solar cells and achieved promising performance in the corresponding devices.

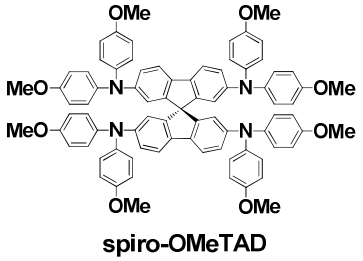

spiro-OMeTAD

Fig. 10. The chemical structure of **spiro-OMeTAD**

5.1 HTMs based on small molecules

5.1.1 Small molecules based on phenylamine derivatives

Due to the great success achieved in **spiro-OMeTAD**-based devices, at present, small molecule HTMs containing phenylamine derivatives, have been widely investigated for application in perovskite solar cells.

Early in 2013, Hodes and coworker employed a small molecule **TPD** as the HTM for perovskite solar cells with $MAPbBr_3$-coated alumina scaffolds and achieved a low PCE of 0.67%.[105] Later, Johansson et al reported a small molecule hole conductor **DEH** for fabricating $MAPbI_3$ perovskite solar cells, and found that, compared with **spiro-OMeTAD**-based device, device with **DEH** showed faster recombination rate (~100 times higher), leading to a decreased performance with a low PCE of 1.6%.[136] The authors suggested that for perovskite solar cells, the molecular structure of the HTM should be designed to block close contact between the perovskite and the hole on the HTM, which is in favor of reducing the electronic coupling and charge recombination. Thus molecule with a bulky, twisty 3-D structure (e.g. phenylamine) may be a potential choice for future HTMs.

In the end of 2013, by replacing the spirobifluorene core of **spiro-OMeTAD** with a pyrene core, three HTMs based on pyrene-core arylamine derivatives, **Py-A**, **Py-B** and **Py-C** was investigated by Seok et al.[137] Comparable *J*sc (~20 mA cm^{-2}) and PCE (~12%) were observed in the cells fabricated with **Py-B** and **Py-C**, while **Py-A**-based device showed low performance (*J*sc =10.8 mA cm^{-2}, PCE = 3.3%), which was due to the insufficient driving force for hole injection from $MAPbI_3$ (-5.44 eV) to **Py-A** (-5.41 eV). Optimal device based on **Py-B** and **Py-C** demonstrated PCEs of 12.3% and 12.4%, repectively, showing the possibility of using new structure HTMs instead of **spiro-OMeTAD** for efficient and low-cost organometal halide perovskite solar cells. Subsequently, a series of dumbbell-shaped or star-shaped molecules with phenylamine derivatives, especially triphenylamine (TPA), as the terminal group or core appeared and some of them exhibited comparable device performance compared with **spiro-OMeTAD**-based perovskite solar cells.

In 2014, Mhaisalkar and coworkers developed two thiophene/TPA-based HTMs **H101**[138] and **KTM3**[139], incorporating 3,4-ethylenedioxythiophene or swivel-cruciform 3,3-bithiophene as the core unit terminated with two or four TPAs. Through appropriate chemical doping with tris(2-(1H-pyrazol-1-yl)pyridine)cobalt(III) tris(hexafluorophosphate) (FK102) (for **H101**) or bis(2,6-di(1H-pyrazol-1-

yl)pyridine)cobalt(III) tris(bis(trifluoromethylsulfonyl)-imide) (FK269) (for **KTM3**), optimal mesoporous devices based on **H101** or **KTM3** achieved PCEs of 13.8% or 11%, respectively under AM 1.5G solar simulation (100 mW cm^{-2}). After that, the authors reported three star-shaped HTMs (**T101**, **T102** and **T103**) based on a rigid triptycene central core.[140] The HOMO levels of **T101**, **T102** and **T103** calculated from CV are -5.29,-5.35 and -5.33 eV, respectively, which are lower than that of **spiro-OMeTAD** (-5.22 eV). By modifying the linkage form between triptycene and diphenylamines groups, devices based on **T101**, **T102** and **T103** yielded PCEs of 8.42%, 12.24% and 12.38%, respectively with relatively high *V*oc. Ko et al also reported two star-shaped HTMs **OMeTPA-TPA** and **OMeTPA-FA** with an incorporated fused quinolizino acridine or TPA as a core unit.[141] Devices comprising FTO/bl-TiO_2/mp-TiO_2/$MAPbI_3$/**OMeTPA-TPA**/Au and FTO/bl-TiO_2/mp-TiO_2/$MAPbI_3$/**OMeTPA-FA**/Au demonstrated PCEs of 12.31% and 13.63% using three dopants composed of 4-tert-butylpyridine (TBP), bis(trifluoromethane)sulfonimide lithium salt (LiTFSI), and tris(2-(1H-pyrazol-1-yl)-4-tert-butylpyridine)cobalt(III) tris(bis(trifluoromethylsulfonyl)imide) (FK209) into the HTMs. A noteworthy feature is that even without any *p*-type additives, a high PCE of 11.7% was still achieved in OMeTPA-FA-based device. Later, Meng and coworker developed two simple HTMs **TPBS** and **TPBC** by introducing electron-donating groups asymmetrically into the N,N,N',N'-tetraphenyl-benzidine core, and achieved impressive PCEs of 10.29% and 13.10% respectively in **TPBS**- and **TPBC**-based devices without any doping.[142]

Recently, Sun and coworkers fabricated FTO/bl-TiO_2/mp-TiO_2/$MAPbI_{3-x}Cl_x$/HTM/Ag-based perovskite solar cells using two carbazole-based small molecules **X19** and **X51** as HTMs.[143] Almost three times higher hole mobilities than that of **Spiro-OMeTAD** (**X19**:1.19× 10^{-4} cm^2 V^{-1} s^{-1}, **X51**: 1.51× 10^{-4} cm^2 V^{-1} s^{-1}, **Spiro-OMeTAD**: 5.31× 10^{-5} cm^2 V^{-1} s^{-1}) were measured for these two materials. Optimal devices with **X19** and **X51** HTMs yielded PCEs of 7.6% and 9.8% under AM 1.5 G (100 mW cm^{-2}) illumination. Lee et al reported the synthesis and characterization of three carbazole-based HTMs with two-arm and three-arm type structures **SGT-404**. **SGT-405** and **SGT-407**, which are linked through phenylene, diphenylene or triphenyl amine derived core units.[144] FTO/bl-TiO_2/mp-TiO_2/$MAPbI_3$/HTM/Au-based devices yielded high efficiencies of 13.28% (**SGT-404**), 14.79% (**SGT-405**) and 13.86% (**SGT-407**), which were comparable to that of the device employing commercial **spiro-OMeTAD** (15.23%).

Xiao and coworkers synthesized a series of HTMs based on a diphenyl core with TPA as terminal group bridged with different length olefinic bonds, which is the first case for the adoption of small molecule HTMs with a linear π-conjugated structure.[145] Without any dopant for HTMs, the FTO/TiO_2/$MAPbI_3$/**2TPA-2-DP**/Au solar cell exhibits an encouraging PCE of 9.1%, with a *V*oc of 0.94 V, a *J*sc of 16.3 mA cm^{-2}, and a FF of 0.597. Meng et al reported two TPA-based hole conductors **HTM1** and **HTM2** containing butadiene derivatives.[146] Both of them exhibited high hole mobilities, which are 2.98 × 10^{-3} cm^2 V^{-1} s^{-1} for **HTM1** and 1.27× 10^{-3} cm^2 V^{-1} s^{-1} for **HTM2**. $MAPbI_3$ perovskite solar cells showed a PCE of 11.34% for **HTM1** and 11.63% for **HTM2**, respectively. Later, the authors employed another low-cost, non-traditional TPA-based HTM **PNBA** in FTO/bl-TiO_2/mp-TiO_2/$MAPbI_3$/**PNBA**/Au-based devices and achieved a PCE of 11.4%.[147]

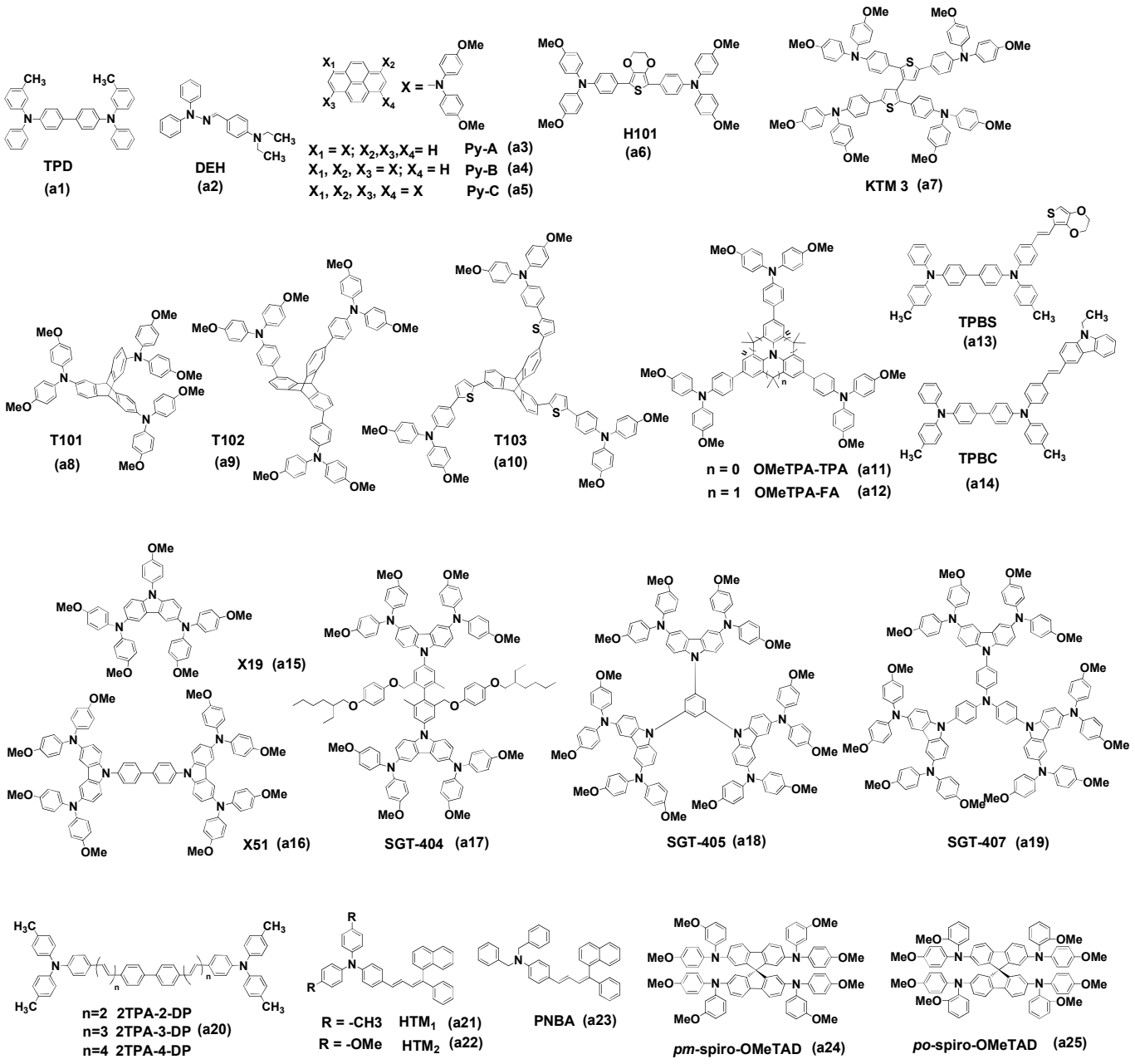

Fig. 11. A summary of small molecule HTMs based on phenylamine derivatives

Besides looking for alternative HTMs with new structures, studied based on the classic **spiro-OMeTAD**, such as structure optimization or energy level engineering are still needed. In 2014, Seok et al synthesized and reported another two **spiro-OMeTAD** isomers by replacing pareb (*p*)-OMe groups in **spiro-OMeTAD** (***pp*-spiro-OMeTAD**) with ortho (*o*)- and meta (*m*)-OMe groups (which are named as ***po*-spiro-OMeTAD** and ***pm*-spiro-OMeTAD**, respectively; see Figure 11).[60] Similar *J*sc and *V*oc were observed for the three ***pp*-**, ***pm*-**, and ***po*-spiro-OMeTAD** derivatives while ***po*-spiro-OMeTAD** showed the highest FF value which can be attributed to its low series resistance (R_s) and shunt resistance (R_{sh}). As a result, a higher PCE of 16.7% was obtained for ***po*-spiro-OMeTAD**-based device compared with the classic ***pp*-spiro-OMeTAD** with a PCE of ~15%. Leo and coworkers used five TPA-based HTMs (including **MeO-TPD**, **spiro-MeO-TPD**, **spiro-TTB**, **spiro-TAD** and **BPAPF**) with **spiro-OMeTAD** to correlate their HOMO energy levels with the *V*oc of the inverted planar $MAPbI_{3-x}Cl_x$-based devices, and highlighted the delicate energetic balance between driving force for hole-extraction and maximizing the photovoltage (see Figure 12).[148]

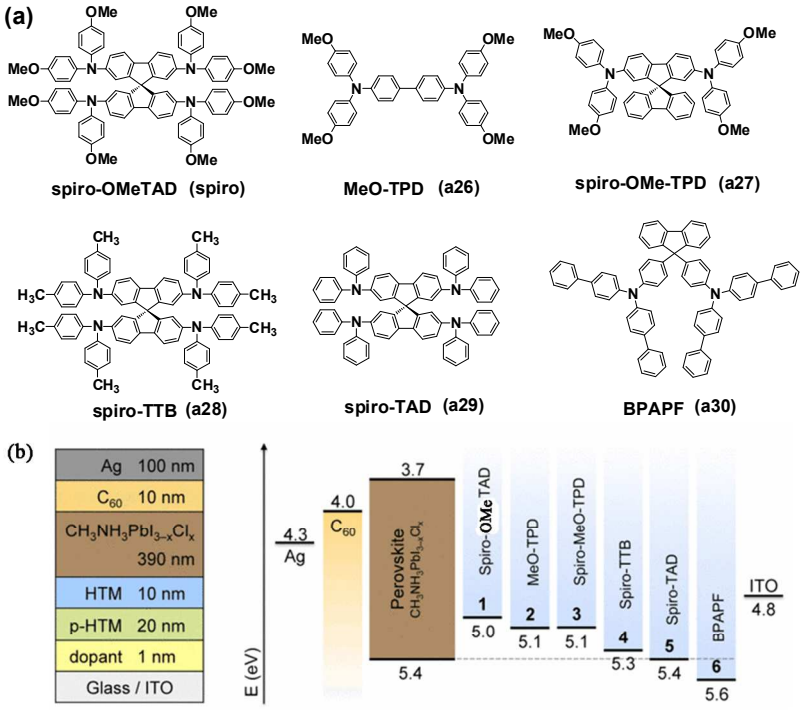

Fig. 12. (a) Chemical structures of HTMs reported by Leo et al. (b) General device architecture and corresponding energylevel diagram. Reprinted with permission.[148]

5.1.2 Small molecules without phenylamine derivatives

Compared with the rapid development of small molecule HTMs containing phenylamine derivatives, studies on non-phenylamine derivatives-based HTMs are relatively little. Earlier reports in 2013 using **PDI**[105], **PC60BM**[105] or **CBP**[149] as HTMs exhibited very low device performances (PCE< 3%). Nowadays, studies on the phenylamine-free small molecule HTMs are mainly focused on the linear or branched conjugated structures. These class of materials always show high hole mobilitiy and good light harvesting ability, and some of them even afford additional contribution to the photocurrent generation of the perovskite solar cells.[150,151]

In 2014, Han and coworkers employed a alkyl-substituted tetrathiafulvalene **TTF-1** as the HTM for $MAPbI_3$-based device.[152] The long alkyl chains in TTF-1 not only improve its solubility for solution processes, but also keep a certain amount of intermolecular stacking due to the fastener-effect of the long alkyl chains. No *p*-type dopants were added, and FTO/bl-TiO_2/mp-TiO_2/$MAPbI_3$/**TTF-1**/Ag-based devices yielded a PCE of 11.03%, with a *J*sc of 19.9 mA cm^{-2}, a *V*oc of 0.86 V, and a FF of 0.644.

Xiao et al reported a low band gap oligothiophene HTM named **DR3TBDTT**, containing benzodithiophene as the central block and ethylrhodanine as the end group.[120] No ion additive was mixed into **DR3TBDTT** but with a small amount addition of insulated polydimethylsiloxane (PDMS), which acted as a flow agent to improve the film forming of HTM on perovskites. Optimal PHJ devices with a FTO/bl-TiO_2/$MAPbI_{3-x}Cl_x$/**DR3TBDTT**/Au structure yielded a PCE of 8.8% with excellent stability. Grätzel et al also developed another two S, N-heteroacene-based dopant-free oligothiophenes **G1** and **G2** as HTMs for FTO/bl-TiO_2/mp-TiO_2/$MAPbI_3$/HTM/Au–based perovskite solar cells, and achieved PCEs of 10.5% and 9.5%, respectively.[150] Nazeeruddin and coworkers synthesized a flattened star-shaped molecule **Fused-F** with quinolizino acridine as core.[151] Device based on **Fused-F** achieved a high PCE of 12.8% under the illumination of 98.8 mW cm^{-2}, with a *V*oc of 1.04 V, a *J*sc of 17.9 mA cm^{-2}, and a FF of 0.68 without any additives.

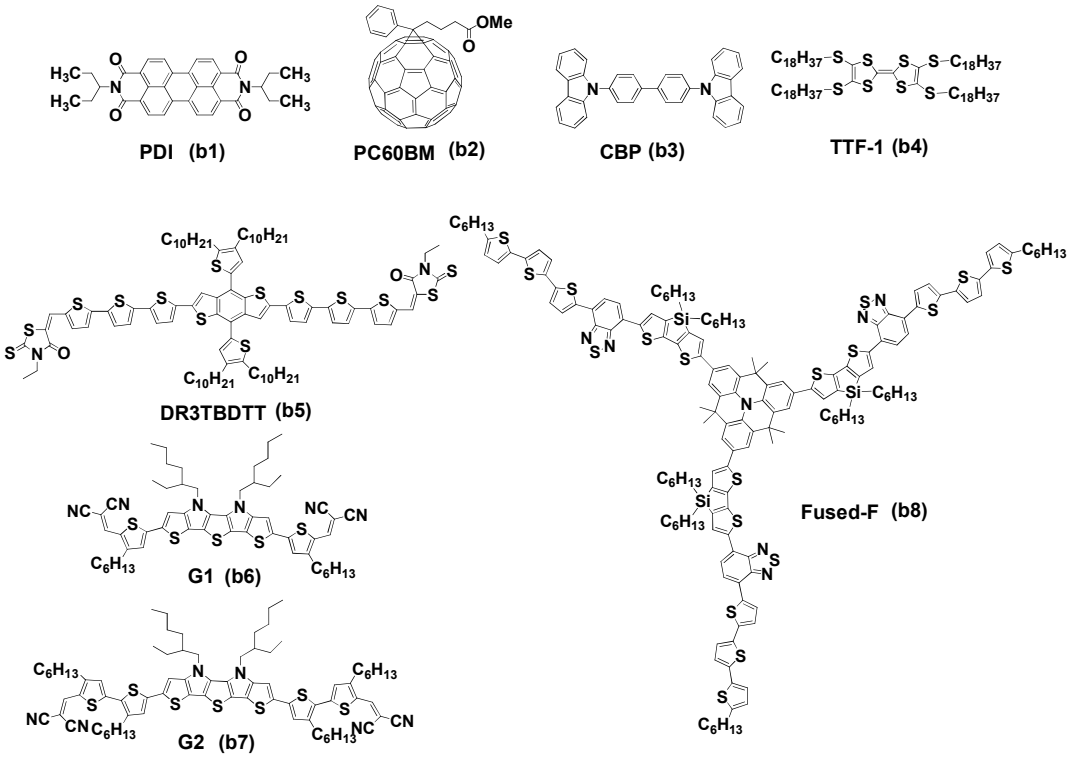

Fig. 13. A summary of small molecule HTMs without phenylamine derivatives

Table 6. A summary of published representative results of small molecule HTM-based device performance parameters with different device fabrication methods and configurations

HTM	E_{HOMO} (eV)	*p*-doping	Device structure	DP	*J*sc (mA/cm^2)	*V*oc (V)	FF (%)	PCE (%)	Ref.
a1	-5.3	NA	FTO/bl-TiO_2/mp-Al_2O_3/$MAPbBr_3$/**a1**/Au	OSPD	1.22	1.20	46	0.67	105
a2	NA	LiTFSI/TBP	FTO/bl-TiO_2/mp-TiO_2/$MAPbI_3$/**a2**/Au	OSPD	NA	NA	NA	1.6	136
a3	-5.41	LiTFSI/TBP/FK209	FTO/bl-TiO_2/mp-TiO_2/$MAPbI_3$/**a3**/Au	OSPD	10.8	0.89	34.6	3.3	137
a4	-5.25	LiTFSI/TBP/FK209	FTO/bl-TiO_2/mp-TiO_2/$MAPbI_3$/**a4**/Au	OSPD	20.4	0.95	63.7	12.3	
a5	-5.11	LiTFSI/TBP/FK209	FTO/bl-TiO_2/mp-TiO_2/$MAPbI_3$/**a5**/Au	OSPD	20.2	0.89	69.4	12.4	
a6	-5.16	LiTFSI/TBP/FK102	FTO/bl-TiO_2/mp-TiO_2/$MAPbI_3$/**a6**/Au	SDP	20.5	1.04	65	13.8	138
a7	-5.29	LiTFSI/TBP/FK269	FTO/bl-TiO_2/mp-TiO_2/$MAPbI_3$/**a7**/Au	SDP	13.0	1.08	78.3	11.0	139
a8	-5.29	LiTFSI/TBP/FK102	FTO/bl-TiO_2/mp-TiO_2/$MAPbI_3$/**a8**/Au	SDP	13.5	0.996	62.6	8.42	140
a9	-5.35	LiTFSI/TBP/FK102	FTO/bl-TiO_2/mp-TiO_2/$MAPbI_3$/**a9**/Au	SDP	17.2	1.03	69.1	12.24	
a10	-5.33	LiTFSI/TBP/FK102	FTO/bl-TiO_2/mp-TiO_2/$MAPbI_3$/**a10**/Au	SDP	20.3	0.985	61.9	12.38	
a11	-5.13	LiTFSI/TBP/FK209	FTO/bl-TiO_2/mp-TiO_2/$MAPbI_3$/**a11**/Au	SDP	20.88	0.946	62	12.31	141
a12	-5.14	LiTFSI/TBP/FK209	FTO/bl-TiO_2/mp-TiO_2/$MAPbI_3$/**a12**/Au	SDP	20.98	0.972	67	13.63	
a13	-5.30	No dopant	FTO/bl-TiO_2/mp-TiO_2/$MAPbI_3$/**a13**/Au	SDP	15.75	0.932	70	10.29	142
a14	-5.33	No dopant	FTO/bl-TiO_2/mp-TiO_2/$MAPbI_3$/**a14**/Au	SDP	19.32	0.942	72	13.10	

a15	NA	LiTFSI/TBP	FTO/bl-TiO_2/mp-TiO_2/$MAPbI_{3-x}Cl_x$ /**a15**/Ag	OSPD	17.14	0.76	58	7.6	143
a16	NA	LiTFSI/TBP	FTO/bl-TiO_2/mp-TiO_2/$MAPbI_{3-x}Cl_x$ /**a16**/Ag	OSPD	16.79	0.88	66	9.8	
a17	NA	LiTFSI/TBP/FK209	FTO/bl-TiO_2/mp-TiO_2/$MAPbI_3$/**a17**/Au	SDP	19.76	0.963	69.8	13.28	144
a18	NA	LiTFSI/TBP/FK209	FTO/bl-TiO_2/mp-TiO_2/$MAPbI_3$/**a18**/Au	SDP	20.28	1.023	71.3	14.79	
a19	NA	LiTFSI/TBP/FK209	FTO/bl-TiO_2/mp-TiO_2/$MAPbI_3$/**a19**/Au	SDP	20.35	0.993	68.6	13.86	
a20	-4.96	No dopant	FTO/bl-TiO_2/mp-TiO_2/$MAPbI_3$/**a20**/Au	OSPD	16.3	0.94	59.7	9.1	145
a21	-5.35	NA	FTO/bl-TiO_2/mp-TiO_2/$MAPbI_3$/**a21**/Au	SDP	18.1	0.921	68	11.34	146
a22	-5.23	NA	FTO/bl-TiO_2/mp-TiO_2/$MAPbI_3$/**a22**/Au	SDP	17.9	0.942	69	11.63	
a23	-5.42	NA	FTO/bl-TiO_2/mp-TiO_2/$MAPbI_3$/**a23**/Au	SDP	17.5	0.945	68.9	11.4	147
a24	-5.31	LiTFSI/TBP	FTO/bl-TiO_2/mp-TiO_2/$MAPbI_3$/**a24**/Au	OSPD	21.1	1.01	65.2	13.9	60
a25	-5.22	LiTFSI/TBP	FTO/bl-TiO_2/mp-TiO_2/$MAPbI_3$/**a25**/Au	OSPD	21.2	1.02	77.6	16.7	
spiro	-5.0	F6-TCNNQ	ITO/dopant/**spiro**/ $MAPbI_{3-x}Cl_x$/**C60**/Ag	DSVD	14.4	0.795	69	7.8	148
a26	-5.1	F6-TCNNQ	ITO/dopant/**a26**/$MAPbI_{3-x}Cl_x$/**C60**/Ag	DSVD	14.9	0.863	69	8.7	
a27	-5.1	F6-TCNNQ	ITO/dopant/**a27**/$MAPbI_{3-x}Cl_x$/**C60**/Ag	DSVD	16	1.03	66	10.9	
a28	-5.3	F6-TCNNQ	ITO/dopant/**a28**/$MAPbI_{3-x}Cl_x$/**C60**/Ag	DSVD	16.1	0.968	70	10.9	
a29	-5.4	F6-TCNNQ	ITO/dopant/**a29**/$MAPbI_{3-x}Cl_x$/**C60**/Ag	DSVD	12.4	0.820	58	6.7	
a30	-5.6	NDP9	ITO/dopant/**a30**/$MAPbI_{3-x}Cl_x$/**C60**/Ag	DSVD	0.72	0.835	13	0.08	
b1	-5.8	NA	FTO/bl-TiO_2/mp-Al_2O_3/$MAPbBr_3$/**b1**/Au	OSPD	1.08	1.30	40	0.56	105
b1	-5.8	NA	FTO/bl-TiO_2/mp-TiO_2/$MAPbBr_3$/**b1**/Au	OSPD	1.14	1.00	41	0.47	
b2	-6.1	NA	FTO/bl-TiO_2/mp-Al_2O_3/$MAPbBr_3$/**b2**/Au	OSPD	1.57	1.06	43	0.72	
b3	-6.23	LiTFSI/TBP	FTO/bl-TiO_2/mp-Al_2O_3/$MAPbBr_{3-x}Cl_x$ /**b3**/Au	OSPD	4.0	1.50	46	2.7	149
b4	-5.05	No dopant	FTO/bl-TiO_2/mp-TiO_2/$MAPbI_3$/**b4**/Ag	SDP	19.9	0.86	64.4	11.03	152
b5	-5.39	PDMS	FTO/bl-TiO_2/$MAPbI_{3-x}Cl_x$ /**b5**/Au	SDP	15.3	0.95	60	8.8	120
b6	-5.26	No dopant	FTO/bl-TiO_2/mp-TiO_2/$MAPbI_3$/**b6**/Au	SDP	16.4	0.992	65	10.5	150
b7	-5.10	No dopant	FTO/bl-TiO_2/mp-TiO_2/$MAPbI_3$/**b7**/Au	SDP	15.2	0.90	68	9.5	
b8	-5.23	No dopant	FTO/bl-TiO_2/mp-TiO_2/$MAPbI_3$/**b8**/Au	SDP	17.9	1.04	68	12.8	151

5.2 HTMs based on polymers

As **spiro-OMeTAD** is the model material in small molecule HTMs, **P3HT** is the model material in polymer HTMs. In previous reports, low PCEs less than 1% were obtained by Hodes and Qiu et al in the mp-TiO_2/$MAPbBr_3$/**P3HT**/Au- or mp-Al_2O_3/$MAPbBr_3$/**P3HT**/Au-based devices.[105,153] Later, by using $MAPbI_3$ or $MAPbI_{3-x}Cl_x$ instead of $MAPbBr_3$ as the active layer, PCEs from 6.7% to over 13% were achieved by several groups, [20,63,64,154-157] showing that **P3HT** can be a suitable HTM for efficient and low cost perovskite based solar cells. Bian and coworkers also used a thin polythiophene film prepared *via* electrochemical polymerization as the HTM in an

ITO/**PT**/$MAPbI_3$/**C60**/BCP/Ag-based device, and observed a PCE of 11.8%.[135]

In 2013, Seok and coworkers reported the use of **PTAA** as the hole conductor for perovskite solar cells.[20] A pillared structure consisting of 3-D composites of TiO_2/$MAPbI_3$ with partially infiltrated **PTAA** was observed and the optimized solar cell device based on FTO/bl-TiO_2/mp-TiO_2/$MAPbI_3$/**PTAA**/Au exhibited a *J*sc of 16.5 mA cm^{-2}, a *V*oc of 0.997 V and a FF of 0.727, yielding a PCE of 12.0% under standard AM 1.5 condition. Subsequently, another two triarylamine polymer derivatives containing fluorene and indenofluorene, named **PF8-TAA**, and **PIF8-TAA**, combined with **PTAA**, were studied to understand and optimize the *V*oc of the result perovskite solar cells with an architecture consisting of FTO/TiO_2/$MAPbBr_3$/HTM/Au or FTO/TiO_2/$MAPbI_3$/HTM/Au.[158] Both the perovskite materials and the HOMO level of the HTM determine the high voltage output and at last, a PCE of 6.7% with a high *V*oc of 1.40 V was obtained in **PIF8-TAA**-based $MAPbBr_3$ perovskite solar cells, which is the highest PCE reported for $MAPbBr_3$ perovskite solar cells. Also, the PCE of the **PTAA**/$MAPbI_3$-based device was further improved to16.2%. Later, Yang and coworkers reported three polyfluorene derivatives, named **PFO**, **TFB** and **PFB**, as the HTMs in $MAPbI_3$-based devices. Highest hole extraction rate of **TFB** was observed and optimal device (FTO/bl-TiO_2/mp-TiO_2/$MAPbI_3$/**TFB**/Au) yielded a PCE of 10.92% and 12.8% *via* OSPD and SDP technique.[159] Grätzel et al also developed a novel 2,4-dimethoxy-phenyl substituted triarylamine oligomer **S197** as the HTM for FTO/bl-TiO_2/mp-TiO_2/$MAPbI_3$/**S197**/Au-based device, and achieved comparable PCE (12%) with **PTAA**-based devices.[160]

Conjugated donor-accepter (D-A) copolymers are widely used in OPVs. D-A Polymers with high hole mobility and appropriate HOMO level can be potential HTM materials for perovskite solar cells. Seok et al fabricated $MAPbI_3$ perovskite solar cells with D-A copolymers **PCPDTBT** or **PCDTBT** as HTM, in which benzothiadiazole as the acceptor and carbazole or cyclopentadithiophene as the donor.[20] A PCE of 4.2% (*J*sc = 10.5 mA cm^{-2}, *V*oc = 0.92 V, FF = 0.437) was observed for **PCDTBT** and a PCE of 5.3% (*J*sc = 10.3 mA cm^{-2}, *V*oc = 0.77 V, FF = 0.667) was observed for **PCPDTBT** in FTO/bl-TiO_2/mp-TiO_2/$MAPbI_3$/HTM/Au-based devices.

Qiu and Park et al reported two diketopyrrolopyrrole-containing polymer HTMs **PCBTDPP** and **PDPPDBTE**. PCEs of 5.55% and 9.2% were obtained respectively by using a FTO/TiO_2/$MAPbI_3$/HTM/Au structure at a 100 mA cm^{-2} illumination (AM 1.5G);[153,161] and it is worth noting that without encapsulation, devices containing **PCBTDPP** or **PDPPDBTE** showed excellent long-term stability in air at room temperature, guaranteeing the practical applicability of these solid-state hybrid solar cells under outdoor working conditions.

Park and coworker also investigated two D-A polymer HTMs **PTB-BO** and **PTB-DCB21** and found that[162], compared with **PTB-BO** without a 3,4-dichlorobenzyl group, the introduction of functionalized **PTB-DCB21** was more effective in accelerating electron transport and retarding charge recombination. As a result, in the condition of without any additives, higher PCE of 8.7% was achieved for **PTB-DCB21**-based devices while PTB-BO-based devices showed a PCE of 7.4%. Recently, Lee et al fabricated a PHJ perovskite solar cell using **PTB7-Th** as the HTM. Devices using an ITO/bl-ZnO/**PC60BM**/$MAPbI_3$/**PTB7-Th**/MoO_3/Ag structure yielded a PCE of 11.04%, with a *J*sc of 15.1 mA cm^{-2}, a *V*oc of 1.03 V, and a FF of 0.71.[118]

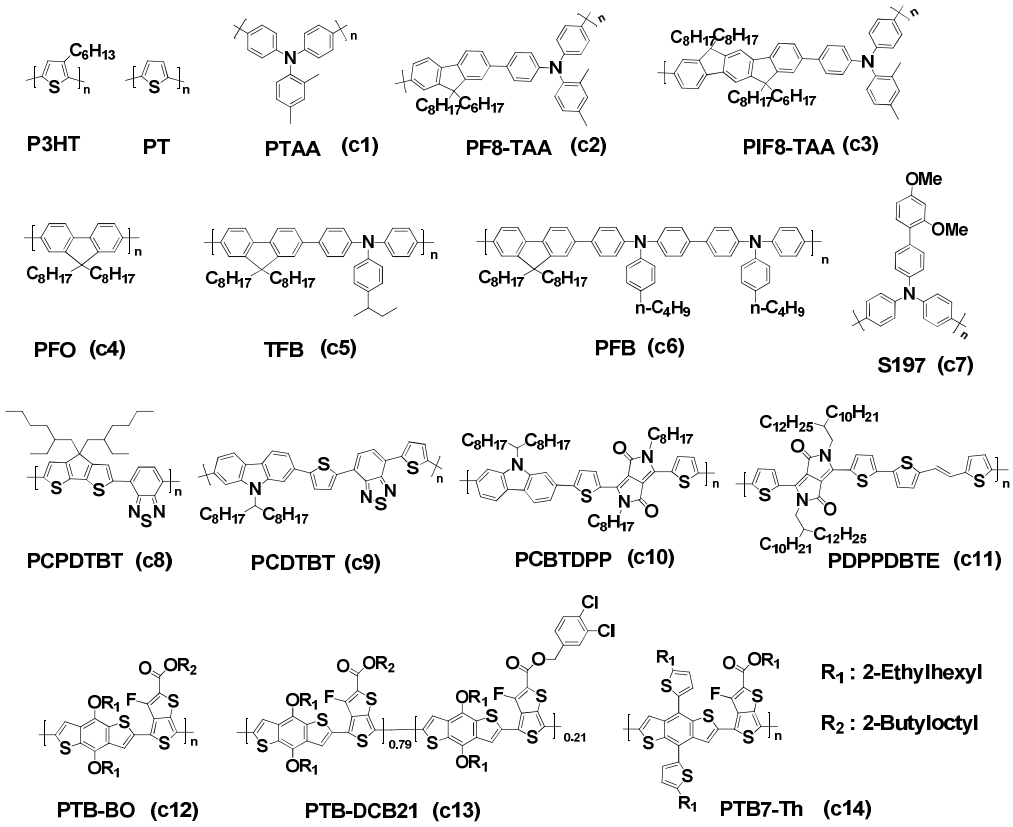

Fig. 9. A summary of polymer HTMs

However, although the wide absorption of low band gap polymers, it has been proven that the role of polymers is only limited to a charge transporting layer rather than as a light harvester because no obvious contribution to external quantum efficiency is found in the long wavelength range. Recently, Snaith and coworkers combined a $MAPbI_{3-x}Cl_x$ perovskite with a fullerene selfassembled monolayer (**C60SAM**) functionalizd TiO_2 to produce a dual absorbing, perovskite−polymer HTM hybrid solar cell (see Figure 14).[163] In this case, electron transfer from the perovskite to the TiO_2 can be blocked and the *V*oc loss reduced. The **C60SAM** acts as a very effective electron acceptor from the perovskite and the polymer HTM, additionally providing polymer photoactivation. With **C60SAM** fullerene functionalization, an increased PCE from 0.17% to 0.43% was observed in no-perovskite devices containing **P3HT**. $MAPbI_{3-x}Cl_x$ perovskite solar cells based on **P3HT** or **PCPDTBT** showed increased PCE from 3.8% to 6.7% or 0.58% to 6.84%, respectively.

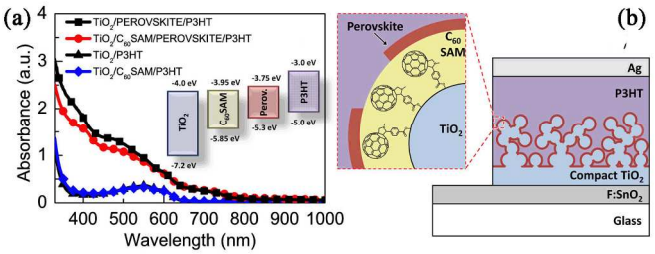

Fig. 14. (a) Absorption spectra of **P3HT** and perovskite films with and without **C60SAM** fullerene functionalization. (b) The schematic of device structure. Reprinted with permission.[163]

Table 7. A summary of published representative results of polymer HTM-based device performance parameters with different device fabrication methods and configurations

HTM	E_{HOMO} (eV)	*p*-doping	Device structure	DP	*J*sc (mA/cm^2)	*V*oc (V)	FF (%)	PCE (%)	Ref.
c1	-5.2	LiTFSI/TBP	FTO/bl-TiO_2/mp-TiO_2/$MAPbI_3$/**c1**/Au	OSPD	16.5	0.997	72.7	12	20
c1	-5.2	LiTFSI/TBP	FTO/bl-TiO_2/mp-TiO_2/$MAPbBr_3$/**c1**/Au	OSPD	6.6	1.29	70	5.9	158
c2	-5.44	LiTFSI/TBP	FTO/bl-TiO_2/mp-TiO_2/$MAPbBr_3$/**c2**/Au	OSPD	6.3	1.36	70	6.0	
c2	-5.44	LiTFSI/TBP	FTO/bl-TiO_2/mp-TiO_2/$MAPbI_3$/**c2**/Au	OSPD	8.9	0.92	56	4.6	
c3	-5.51	LiTFSI/TBP	FTO/bl-TiO_2/mp-TiO_2/$MAPbBr_3$/**c3**/Au	OSPD	6.1	1.40	79	6.7	
c3	-5.51	LiTFSI/TBP	FTO/bl-TiO_2/mp-TiO_2/$MAPbI_3$/**c3**/Au	OSPD	19.0	1.04	46	9.1	
c4	-5.8	LiTFSI/TBP	FTO/bl-TiO_2/mp-TiO_2/$MAPbI_3$/**c4**/Au	OSPD	3.6	0.61	56	1.22	159
c5	-5.3	LiTFSI/TBP	FTO/bl-TiO_2/mp-TiO_2/$MAPbI_3$/**c5**/Au	OSPD	17.5	0.96	65	10.92	
c5	-5.3	LiTFSI/TBP	FTO/bl-TiO_2/mp-TiO_2/$MAPbI_3$/**c5**/Au	SDP	NA	NA	NA	12.8	
c6	-5.1	LiTFSI/TBP	FTO/bl-TiO_2/mp-TiO_2/$MAPbI_3$/**c6**/Au	OSPD	13.8	0.91	64	8.03	
c7	-5.12	LiTFSI/TBP	FTO/bl-TiO_2/mp-TiO_2/$MAPbI_3$/**c7**/Au	SDP	17.6	0.967	70	12	160
c8	-5.3	LiTFSI/TBP	FTO/bl-TiO_2/mp-TiO_2/$MAPbI_3$/**c8**/Au	OSPD	10.3	0.77	66.7	5.3	20
c9	-5.45	LiTFSI/TBP	FTO/bl-TiO_2/mp-TiO_2/$MAPbI_3$/**c9**/Au	OSPD	10.5	0.92	43.7	4.2	
c10	-5.4	No dopant	FTO/bl-TiO_2/mp-TiO_2/$MAPbBr_3$/**c10**/Au	OSPD	4.47	1.16	59	3.04	153
c10	-5.4	No dopant	FTO/bl-TiO_2/mp-TiO_2/$MAPbI_3$/**c10**/Au	OSPD	13.86	0.83	48	5.55	
c11	-5.4	LiTFSI/TBP	FTO/bl-TiO_2/mp-TiO_2/$MAPbI_3$/**c11**/Au	OSPD	14.4	0.855	74.9	9.2	161
c12	-5.22	No dopant	FTO/bl-TiO_2/mp-TiO_2/$MAPbI_3$/**c12**/Au	OSPD	14.35	0.827	62	7.4	162
c13	-5.25	No dopant	FTO/bl-TiO_2/mp-TiO_2/$MAPbI_3$/**c13**/Au	OSPD	15.35	0.888	64	8.7	
c14	-5.22	No dopant	ITO/bl-ZnO/**PC60BM**/$MAPbI_3$/**c14**/MoO_3/Ag	SDP	15.1	1,03	71	11.04	118
P3HT	-5.2	No dopant	FTO/bl-TiO_2/mp-TiO_2/**P3HT**/Ag	-	0.69	0.42	58	0.17	163
P3HT	-5.2	No dopant	FTO/bl-TiO_2/mp-TiO_2/**C60SAM**/**P3HT**/Ag	-	1.6	0.5	55	0.43	
P3HT	-5.2	No dopant	FTO/bl-TiO_2/mp-TiO_2/$MAPbI_{3-x}Cl_x$/**P3HT**/Ag	OSPD	10.1	0.68	55.3	3.8	
P3HT	-5.2	No dopant	FTO/bl-TiO_2/mp-TiO_2/**C60**SAM/ $MAPbI_{3-x}Cl_x$/**P3HT**/Ag	OSPD	14.9	0.81	55.5	6.7	
c8	-5.3	No dopant	FTO/bl-TiO_2/mp-TiO_2/$MAPbI_{3-x}Cl_x$/**c8**/Ag	OSPD	5.02	0.3	40	0.58	
c8	-5.3	No dopant	FTO/bl-TiO_2/mp-TiO_2/**C60**SAM/$MAPbI_{3-x}Cl_x$/**c8**/Ag	OSPD	15.6	0.88	51	6.84	

5.3 HTMs based on inorganics

Compared with organic HTMs, inorganic *p*-type semiconductors appear to be an ideal choice due to their high mobility, stability, ease of synthesis and low cost. However, up to now, the study on inorganic HTM for perovskite solar cells is very limited. In 2013, Kamat and coworkers reported a FTO/bl-TiO_2/mp-TiO_2/$MAPbI_3$/CuI/Au structure device using CuI as HTM and achieved a PCE of 6%, with a relatively lower *V*oc of 0.55 V compared to that (0.79 V) of device with **spiro-OMeTAD**.[164] The authors attributed this to the higher recombination in CuI-based device and this research highlighted the direction to develop all-inorganic materials for perovskite-based photovoltaic devices. Subsequently, Sarkar,[132] Ito[165,166], Tena-Zaera[121] and Nazeeruddin[167] et al independently fabricated conventional or inverted device based on CuSCN HTM and reached PCE from 3.8% to 12.4%.

Inspired by the application of NiO layer in polymer bulk-heterojunction solar cells,[168,169] Guo and Sarkar et al developed a series of perovskite-based mesoscopic or PHJ solar cells using spin-coated NiO_x thin film,[102] NiO nanocrystalline[101, 104]or electrodeposited NiO film[132] on a glass/ITO or FTO electrode as HTM, and PCE increased from 5.7% to 11.6% was obtained at last.

5.4 HTM-free perovskite solar cells

Apart from the widely used TiO_2/perovskite/HTM configuration, another configuration, in which *n*-type metal oxides combine with perovskites to form a *p*–*n* junction without additional HTMs was developed. Organometal halide perovskite acts both as a light harvester and as a hole conductor simultaneously. Elimination of the hole conductor can improve the stability, lower the cost and simplify the fabrication process.

In 2012, Etgar and coworkers firstly reported a HTM-free perovskite solar cell with a FTO/bl-TiO_2/mp-TiO_2/$MAPbI_3$/Au structure using TiO_2 (anatase) nanosheets as the electron collector.[14] Device based on this simaple $MAPbI_3$ perovskite/TiO_2 heterojunction showed a promising PCE of 5.5%, with a *J*sc of 16.1 mA cm^{-2}, a *V*oc of 0.63 V, and a FF of 0.57 under standard AM 1.5 solar light of 100 mW cm^{-2} intensity. Subsequently, the authors further improved the photovoltaic performance to 8%[170] then to 10.85%[171] through the optimization of the $MAPbI_3$ perovskite film formation[54]. In 2014, Etgar et al introduced Br- ions into the perovskite structure to construct $MAPbI_nBr_{3-n}$ (where $0 \leqslant n \leqslant 3$) as hole conductor and light harvester in the solar cell.[172] Compared to the pure $MAPbI_3$ which yielded a PCE of 7.2%, perovskite film with the molar ratio of MABr to MAI (in the dip solution) as 1:2 exhibited a PCE of 8.54% with improved stability.

Considering the existed Schottky contact at the metal−semiconductor interface between $MAPbI_3$ and Au, in 2013, Meng et al deposited an ultrathin Al_2O_3 insulator layer on a $MAPbI_3$ layer to construct a metal−insulator−semiconductor back contact and an enhanced PCE from 3.30% to 5.07% was obtained.[173] Later, they developed a simple solution process to engineer the M−S interface using a thin wide band gap organic semiconductor N,N,N′,N′-tetraphenyl-benzidine layer, yielding an enhanced PCE from 5.26% to 6.71%.[174] In 2014, using an ideal model for a single heterojunction solar cell, Meng and coworkers confirmed the heterojunction nature of the TiO_2/$MAPbI_3$/Au cell and improve PCEs to over 10% with high *V*oc over 0.9 V in a HTM-free perovskite system.[42,175] Recently, by the *in situ* preparation of perovskite sensitized photoanode, Xiao et al also achieved PCEs of 9.03%[87] and 10.03%[176] in a TiO_2 nanofiber- and TiO_2 nanoparticle-based device. Zhang et al deposited $MAPbI_3$ on the oriented rod-type TiO_2 by a solvothermal process and a PCE of 4.2% was obtained with good stability.[65] Kanatzidis et al achieved a PCE of over 10.6% with a negligible standard deviation by depositing $MAPbI_3$ *via* a facile low-temperature (<150 °C), gas−solid crystallization process[177].

The inexpensive and abundantly available carbon (work function: -5.0 eV) may be an ideal material to substitute Au or Ag as a counter electrode (CE) in perovskite solar cells. In 2013, Han and coworkers initially developed a HTM-free fully printable mp-TiO_2/$MAPbI_3$ heterojunction solar cell with low-cost carbon CE.[178] In this device, a double layer of mesoporous TiO_2 and ZrO_2 is firstly deposited on the top of FTO/bl-TiO_2 substrates, followed by the printing of a porous carbon black/graphite composite as the CE (see Figure 15a). The inserted ZrO_2 layer acts as an insulating layer to prevent short circuit. Then the $MAPbI_3$ perovskite is infiltrated into the porous TiO_2/ZrO_2 scaffold by drop-casting a solution through the printed carbon layer. The authors selected two type carbon CEs including carbon black/flaky graphite (FG) composite and carbon black/spheroidal graphite (SG) composite to fabricate devices, and achieved PCEs of 4.08% (*J*sc = 10.6 mA cm^{-2}, *V*oc = 0.825 V, FF = 0.46) and 6.64% (*J*sc = 12.4 mA cm^{-2}, *V*oc = 0.878 V, FF = 0.61), respectively. The main difference in FF can be attributed to the different morphology of FG- and SG-based CEs. In the FG-based device, large graphite sheets were stacked on the top of ZrO_2, while a loose structure was observed in SG-based CE, which is more beneficial to the pore-filling of $MAPbI_3$ in the TiO_2 films. Later, *via* optimization of the carbon CEs[179] (e.g. ordered mesoporous carbon/FG), TiO_2 nanostructure[80] (e.g. TiO_2 nanosheets), perovskite deposition method[80] or perovskite structure[180,181] (e.g. $(5\text{-AVA})_x(MA)_{1-x}PbI_3$ or $(FA)_x(MA)_{1-x}PbI_3$), higher PCE up to ~13% was yielded, which is the highest reported value for HTM-free perovskite solar cells. Zhao et al also replaced the insulating ZrO_2 with the *p*-type mesoscopic NiO, and observed enhanced performances in TiO_2/mp-NiO($MAPbI_3$)/carbon-based device (*J*sc = 18.2 mA cm^{-2}, *V*oc = 0.89 V, FF = 0.71, PCE = 11.4%) compared with the TiO_2/mp-ZrO_2($MAPbI_3$)/carbon-based device (*J*sc = 16.4 mA cm^{-2}, *V*oc = 0.818 V, FF = 0.60, PCE = 8.2%), which was attributed to the enlarged electron lifetime and the augmented interfacial charge transfer process on the carbon counter electrode.[182]

Yang[183] and Ma[184] also reported a low-temperature-processed carbon CE-based device with a conventional FTO/bl-TiO_2/mp-TiO_2/$MAPbI_3$/carbon CE structure at the same time. Similar PCE of 8.31% and 9.08% were achieved and both devices demonstrated good stability (see Figure 15b). Later, slightly higher PCE of 10.2% was reported by Meng et al in similar device, in which the counter electrode contained a composition of graphite and carbon black.[185] Recently, by using the inkjet printing technique, the first example of planar carbon-based perovskite solar cell FTO/bl-TiO_2/$MAPbI_3$/carbon was fabricated.[186] Unlike the traditional perovskite deposition *via* OSPD or SDP, a reactive ink mixing carbon black and MAI in isopropanol was directly printed on the top of FTO/bl-TiO_2/PbI_2-based devices, leading to a quick chemical transformation *in situ* and significantly improving carbon/$MAPbI_3$ interface. Also, another noteworthy feature is the precisely controlled pattern of the carbon electrodes. As a result, a PCE of 11.60% was achieved, with a *J*sc of 17.2 mA cm^{-2}, a *V*oc of 0.95 V, and a FF of 0.71.

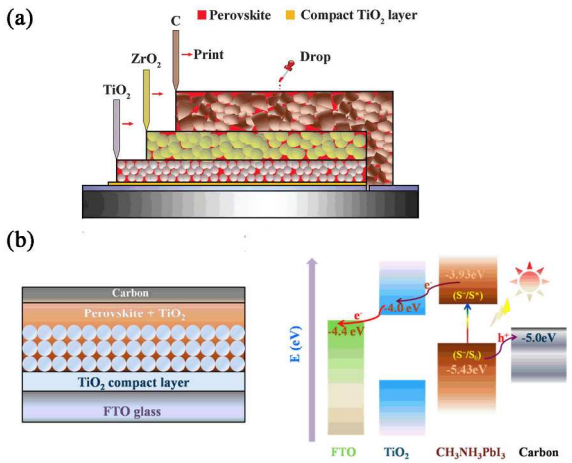

Fig. 15. (a) The schematic structure of a carbon based monolithic device. Reprinted with permission.[181](b) Device architecture and energy levels (relative to vacuum) of various device components. Reprinted with permission.[183]

6. Perovskite structure engineering

6.1 Bromine (Br)- based organic–inorganic halide perovskite

For methylammonium lead halide perovskite ($MAPbX_3$), the tuning of the halide in X position from Cl to Br and I can effectively broaden the absorption spectrum, with a decreased E_g from 3.11[187] to 2.3[188] and 1.50 eV[12]. At present, two type perovskites including the single halide perovskite (typically $MAPbI_3$ or $MAPbBr_3$) and the mixed halide perovskite (typically $MAPbI_{3-x}Cl_x$, $MAPbI_{3-x}Br_x$ or $MAPbBr_{3-x}Cl_x$) have been applied in perovskite solar cells. Especially, devices with $MAPbI_3$ or $MAPbI_{3-x}Cl_x$ as the active layer have attracted numerous attentions due to their relatively low band gaps (~1.5 eV) and large charge carrier diffusion lengths.[115,116] Excellent ~10% efficiencies were obtained in 2012 from the initial two reports on solid organometal trihalide perovskite solar cells based on $MAPbI_3$[12] or $MAPbI_{3-x}Cl_x$[13]. So far, *via* the optimization of device architecture and perovskite morphology, cells incorporating $MAPbI_3$ or $MAPbI_{3-x}Cl_x$ perovskite have yielded PCE of over 17%[21] and 19%[23].

While great progress has been achieved in $MAPbI_3$-based devices, $MAPbBr_3$-based devices haven't exhibited satisfactory performance. Initial studies on porous TiO_2 or Al_2O_3-based devices using **PDI**, **TPD**, **PC60BM** or **P3HT** as the HTM demonstrated low PCEs of less than 1%,[105,153] then improved to 6.7% efficiency in a FTO/bl-TiO_2/mp-TiO_2/$MAPbBr_3$/**PIF8-TAA**/Au based device (Jsc = 6.1 mA cm^{-2}, Voc = 1.4 V, FF = 0.79)[153,158]. The main reason for this low device performance can be attributed to the wider band gap of $MAPbBr_3$ (2.3 eV) than that of $MAPbI_3$ (1.5 eV), which limits the light harvest and then decreases the short current. However, higher Voc was always observed in $MAPbBr_3$-based devices compared to the referenced $MAPbI_3$-based devices (with the same device architecture), which is due to the lower valence band edge (-5.6 eV) and the higher conduction band edge (-3.4 eV) of $MAPbBr_3$ compared to that of $MAPbI_3$ (-5.4/-3.9), leading to a larger difference between the quasi-Fermi level of the electron and the quasi-Fermi level of the hole in $MAPbBr_3$-based devices. Later, by doping chloride ions in $MAPbBr_3$ films with **CBP** as the HTM, a Voc as high as 1.5 V was obtained in a FTO/bl-TiO_2/mp-Al_2O_3/$MAPbBr_{3-x}Cl_x$/**CBP**/Au-based device, with a Jsc of 4 mA cm^{-2}, a FF of 0.46 and a PCE of 2.7%.[149]

In 2013, Seok and coworkers introduced a work of band gap engineering by the chemical management of perovskites $MAPb(I_{1-x}Br_x)_3$ ($0 \leqslant x \leqslant 1$)[188]. With the increase of Br-concentration (x), the tetragonal phase (I4/mcm) of $MAPbI_3$ gradually transited to a cubic phase ($Pm\bar{3}m$) due to the enhanced symmetry (x >0.2), along with the decrease of the band gap, which was clearly demonstrated in the perovskite films where the color changed from dark brown to brown/red, then to yellow (see Figure 16). In the J–V characteristics of resultant devices with a FTO/bl-TiO_2/mp-TiO_2/$MAPb(I_{1-x}Br_x)_3$/**PTAA**/Au structure, with increasing x from 0 to 1, regularly decreased Jsc and increased Voc were obtained, which was corresponding to the variation of absorption and energy levels. Interestingly, an increase in the fill factor from 0.66 to 0.74 was also measured, indicating the better charge transport properties in Br-doped cells. At last, an average of more than 10% with maximum PCEs of 12.3% were achieved when x varied in the range of 0 to 0.2, and a low sensitivity to the humidity when $x \geqslant 0.2$ was observed (the authors further achieved a higher PCE of up to 16.2% in later reports using solvent engineering in $MAPb(I_{1-x}Br_x)_3$ (x=0.1-0.15)-based devices[24]).

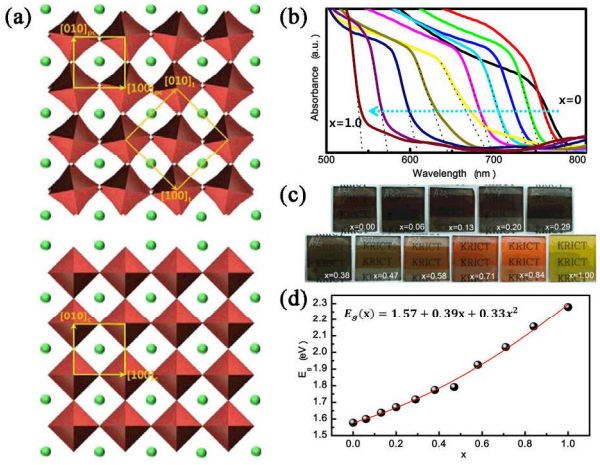

Fig.16 (a) Crystal structures and unit lattice vectors on the (00l) plane of the tetragonal (I4/mcm) (top) and cubic ($Pm\bar{3}m$) (bottom) phases are represented. (b) UV−vis absorption spectra of FTO/bl-TiO_2/mp-TiO_2/$MAPb(I_{1-x}Br_x)_3$/Au cells measured using an integral sphere. (c) Photographs of TiO_2/$MAPb(I_{1-x}Br_x)_3$ bilayer nanocomposites on FTO glass substrates. (d) A quadratic relationship of the band-gaps of $MAPb(I_{1-x}Br_x)_3$ as a function of Br composition (x). Reprinted with permission [188]

Yang and coworkers also fabricated a $MAPbI_2Br$-based mesoporous device by spin-coating a precursor solution of equimolar MABr and PbI_2 on the top of one-dimensional TiO_2 nanowire arrays, and achieved a PCE of 4.87%, with a Jsc of 10.12 mA cm^{-2}, a Voc of 0.82 V, and a FF of 0.59.[83] In 2014, Zhu et al prepared a high-quality $MAPbI_2Br$ film on a planar device by thermal decomposition from a film deposited using a precursor containing PbI_2, MABr, and MACl.[37] The amount of Cl in the film decreases with annealing duration and no trace of Cl was observed at the latter stage of annealing.[36] The incopration of MACl not only effectively adjusted the crystallization process for $MAPbI_2Br$ but also enhanced the absorption of the resultant film. Finally, a compact packing of

nanosheets completely covering the substrate was obtained and device based on FTO/bl-TiO_2/$MAPbI_2Br$/**spiro-MeOTAD**/Ag showed a PCE of 10.03%, with a *J*sc of 14.81 mA cm^{-2}, a *V*oc of 1.09 V, and a FF of 0.62 under the simulated AM 1.5G illumination (100 mW/cm^2).

6.2 Formamidinium (FA)-based organic–inorganic halide perovskite

The first formamidinium (FA) lead trihalide-based perovskite solar cell was reported by Boix and coworkers in the end of 2013,[189] in which the FA cation ($HC(NH_2)^{2+}$) was employed to substitute the conventional MA cation to synthesize $FAPbI_3$. The incorporation of the larger FA cation can effectively lower the band gap of the commonly used $MAPbI_3$ perovskite towards the optimum value of ~1.4 eV (E_g = 1.47 eV), which is beneficial to extended absorption of light and increase the short-circuit current density. Primary device based on FTO/bl-TiO_2/mp-TiO_2/$FAPbI_3$/**spiro-OMeTAD**/Au yielded a PCE of 4.3% (*J*sc = 6.45 mA cm^{-2}, *V*oc = 0.97 V, FF = 0.687),[189] which was further improved to 7.5%[190] in a mesoscopic FTO/bl-TiO_2/mp-TiO_2/$FAPbI_3$/**P3HT**/Au device and 14.2%[191] in a planar FTO/bl-TiO_2/$FAPbI_3$/**spiro-OMeTAD**/Au device. Unlike $MAPbI_3$, the complete conversion of $FAPbI_3$ *via* OSPD always needs a high temperature (>140 °C), which may result in a poor crystal quality $FAPbI_3$ perovskite layer. Thus a SDP method is suitable due to the film fabrication can be proceeded at a low temperature (~100 °C). Snaith et al also reported a method to form uniform and continuous films by adding a small amount of hydroiodic acid (HI) to the precursor solution (FAI : PbI_2 =1:1).[191]The authors thought that the presence of HI could help to solubilize the inorganic component, then slow down the perovskite film crystallization, enabling a smoother film to be formed, without influencing the crystal structure. Another noteworthy feature is that $FAPbI_3$ has two polymorphs, including a black perovskite-type material (*α*- phase) with trigonal symmetry (P3m1), and a yellow hexagonal nonperovskite (*γ*-phase) counterpart (P63mc).[192] In a humid atmosphere at room temperature, the black *α*- phase can quickly and fully convert to the yellow *γ*-phase. For a $FAPbI_3$-based perovakite solar cell, the present of yellow *γ*-phase is an adverse factor to the device performance, however, in most cases, the yellow *γ*-phase can be disappeared at a higher temperature annealing temperature (>100 °C). Later, considering the weak light absorption of $FAPbI_3$ at long wavelength (>700 nm), Park and coworkers introduced a thin $MAPbI_3$ overlayer on the top of the $FAPbI_3$.[193] Enhanced IPCE at long wavelength and modified perovskite/HTM interface brought increased average photocurrent (~2.8%) and photovoltage (~1.9%) compared to the non-$MAPbI_3$ overlayer devices, yielding a high PCE of 16.01%, with an average PCE of 15.56%.

Grätzel and coworker fabricated a mixed-cation perovskite $(MA)_x(FA)_{1-x}PbI_3$ (x=0–1) as the active layer *via* SDP.[194] Devices based on FTO/bl-TiO_2/mp-TiO_2/$MA_{0.6}FA_{0.4}PbI_3$/**spiro-OMeTAD**/Au yielded the highest PCE of 14.9%, with an average PCE of 13.4%, which is higher than pure $FAPbI_3$- (11%) and $MAPbI_3$- (12.5%) based devices. The mixed-cation perovskite $MA_{0.6}FA_{0.4}PbI_3$ could avoid the formation of yellow phase and, interestingly, exhibited the same band gap as $FAPbI_3$. Also, by optimizing the ration of FA and MA cation, a PCE of 12.9% was achieved in a hole-conductor-free -based device with a FTO/bl-TiO_2/mp-TiO_2/ZrO_2/carbon CE/$MA_{0.4}FA_{0.6}PbI_3$ structure.[180] Besides the modification of the organic cation, Cui et al[195] and Docampo et al[196] reported two devices based on $FAPbI_{3-x}Cl_x$ (FTO/bl-TiO_2/mp-TiO_2/ $FAPbI_{3-x}Cl_x$/**P3HT**/Au) and $FAPbBr_3$ (FTO/bl-TiO_2/$FAPbBr_3$/**spiro-OMeTAD**/Au) perovskites, and achieved PCEs of 7.51% and 6.5%.

Table 8. A summary of published representative results of FA-based perovskite solar cell performance parameters with different device fabrication methods and configurations

PL	DP	Device structure	*J*sc (mA/cm^2)	*V*oc (V)	FF (%)	PCE (%)	Ref.
$FAPbI_3$	SDP	FTO/bl-TiO_2/mp-TiO_2/PL/**spiro**/Au	6.45	0.97	68.7	4.3	189
$FAPbI_3$	SDP	FTO/bl-TiO_2/mp-TiO_2/PL/**P3HT**/Au	18.3	0.84	50	7.5	190
$FAPbI_3$	OSPD	FTO/bl-TiO_2/PL/**spiro**/Au	23.3	0.94	65	14.2	191
$FAPbI_3$	SDP	FTO/bl-TiO_2/mp-TiO_2/PL/$MAPbI_3$/**spiro**/Au	20.97	1.032	74	16.01	193
$MA_{0.6}FA_{0.4}PbI_3$	SDP	FTO/bl-TiO_2/mp-TiO_2/PL/**spiro**/Au	21.2	1.003	70	14.9	194
$MA_{0.4}FA_{0.6}PbI_3$	SDP	FTO/bl-TiO_2/mp-TiO_2/ZrO_2/carbon CE/PL	20.9	0.921	67	12.9	180
$FAPbI_{3-x}Cl_x$	OSPD	FTO/bl-TiO_2/mp-TiO_2/PL/**P3HT**/Au	19.24	0.73	54	7.51	195
$FAPbBr_3$	SDP	FTO/bl-TiO_2/PL/**spiro**/Au	6.6	1.35	73	6.5	196

6.3 Tin (Sn)-based organic–inorganic halide perovskite

Sn could be a potential alternative to Pb for organic–inorganic halide perovskite due to the reasons that both of them belong to the IVA group with similar ionic radii. Also, the less toxicity of Sn compared to Pb and the low optical band gap of $MASnI_3$[192,197] (~1.3 eV) compared to $MAPbI_3$ (~1.55 eV) provide an opportunity to develop lead-free solar cells with high efficiencies. In 2014, Ogomi and coworkers firstly fabricated a series of mixed Pb/Sn alloy $MASn_xPb_{1-x}I_3$ perovskites in a FTO/bl-TiO_2/mp-TiO_2/$MASn_xPb_{1-x}I_3$/**P3HT**/Ag/Au-based device.[198] The optimal photovoltaic performance was observed when x was 0.5 ($MASn_{0.5}Pb_{0.5}I_3$), exhibiting a PCE of 4.18%, with a *J*sc of 20.04 mA cm^{-2}, a *V*oc of 0.42 V, and a FF of 0.50 at AM 1.5G one sun illumination. The wide absorption area up to 1060 nm leads to this high *J*sc while the low *V*oc can be attributed to the poor perovskite morphology with flowerlike crystals and the obvious observation of the Sn^{2+} oxidation in the Sn perovskites.[192] Later, Kanatzidis et al also reported a ~7% efficiency, with a ~20 mA cm^{-2} *J*sc in a FTO/bl-TiO_2/mp-TiO_2/$MASn_{0.5}Pb_{0.5}I_3$/**spiro-OMeTAD**/Au device (see Figure 17).[199] Higher PCE of 10.1% was achieved by Jen and coworkers in a planar ITO/PEDOT:PSS/$MAPb_{0.85}Sn_{0.15}I_{3-x}Cl_x$/**PC60BM**/**C60-bis**/Ag-based device, with a *J*sc of 19.5 mA cm^{-2}, a *V*oc of 0.77 V, and a FF of 0.67.[200] Compared with the referential $MAPbI_{3-x}Cl_x$ film with coverage of 87%, the

$MAPb_{0.85}Sn_{0.15}I_{3-x}Cl_x$ film demonstrated an increased coverage (~97%) and excellent continuity due to the Sn's effect on nucleation and growth, which is beneficial to suppress charge recombination and improve transport.

While the good semiconducting behaviour observed in Pb/Sn alloy perovskite-based device, the completely lead-free organic–inorganic tin halide perovskites havn't exhibited inspiring photovoltaic performance, and always with relatively low fill factor (< 60%), which is mainly because of the more significant self-doping in the Sn perovskites. So far, devices based on the different lead-free perovskites $MASnI_3$[199,201] (FTO/bl-TiO_2/mp-TiO_2/$MASnI_3$/**spiro-OMeTAD**/Au), $MASnI_{3-x}Br_x$[202] (FTO/bl-TiO_2/mp-TiO_2/$MASnI_{3-x}Br_x$/**spiro-OMeTAD**/Au), $MASnI_{3-x}Cl_x$[200] (ITO/PEDOT:PSS/$MASnI_{3-x}Cl_x$/**PC60BM**/**C60-bis**/Ag) have yielded PCEs of 6.4%, 5.73%, and 0.04%, respectively.

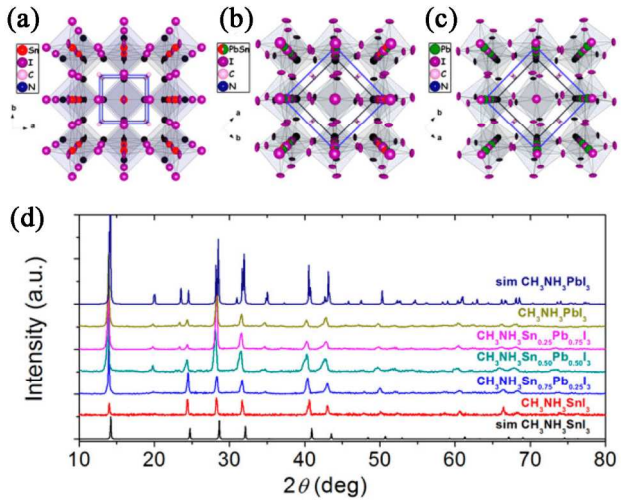

Fig.17 Crystal structure (a, b, and c) and X-ray diffraction pattern (d) of the $MASn_{1-x}Pb_xI_3$ solid solutions. Simulated X-ray diffraction patterns of the two end compositions of $MAPbI_3$ and $MASnI_3$ are also shown in (d). Reprinted with permission[199]

7. Conclusions and Prospects

In this review, we summarize and discuss recent developments about the organometal halide perovskite-based all-solid-state solar cells. With extensive research and accumulated understanding, the unique physical and optoelectronic properties of organometal halide perovskites have been explored and elucidated. The organometal halide perovskites can not only play as the light absorber but also work efficiently in various of device architectures going from a dye sensitized concept due to the bipolar transport of both holes and electrons. For the core part ABX_3 perovskites, (a) reasonable structure engineering based on A (e.g. MA and FA), B (e.g. Pb and Sn), and/or X (e.g. Cl, Br and I) can effectively modify the resultant optical band gaps, the HOMO/LUMO energy levels as well as the charge diffusion length, and finally affects the resultant photovoltaic performance. For example, long electron–hole diffusion lengths exceeding 1 μm for the mixed halide perovskite of $MAPbI_{3-x}Cl_x$ was measured, while it was only 100 nm for the triiodide perovskite of $MAPbI_3$; (b) the morphology and crystals in perovskite films are not only related to the nature of materials, but also can be optimized by carefully modifying the deposition methods (e.g. solution-based deposition and vapor-based deposition) and/or controlling the device fabrication conditions (e.g. thermal annealing, additive treatment and solvent engineering); (c) since in perovskite layers, as well as for most ionic crystals, the coordination number for ions at the crystal surfaces is always lower than in the bulk material, energetic disorderness (i.e., charge traps and structural defects) always exists at the perovskite surface and/or grain boundaries, thus a passivation technique (e.g. IPFB, Lewis base and PbI_2) could be employed to lower carrier recombination rate and improve device performance.

For perovskite solar cells base on a porous structure (MMOPSC and MSSC), the porous scaffold can be conductive metal oxides including *n*-type TiO_2 (17.01%, ITO/bl-TiO_2/mp-TiO_2/$MAPbI_3$/**spiro-OMeTAD**/Au), ZnO (12%, FTO/bl-ZnO(Al)/mp-ZnO(Al)/$MAPbI_3$/HTM/Ag) and *p*-type NiO (11.6%, ITO/bl-NiO_x/mp-NiO/$MAPbI_3$/**PC60BM**/BCP/Al); or insulating materials including Al_2O_3 (15.9%, FTO/bl-TiO_2/mp-Al_2O_3/$MAPbI_{3-x}Cl_x$/**spiro-OMeTAD**/Ag), ZrO_2 (10.8%, FTO/bl-TiO_2/mp-ZrO_2/$MAPbI_3$/**spiro-OMeTAD**/Ag) and SiO_2 (11.45%, FTO/bl-TiO_2/mp-SiO_2/$MAPbI_{3-x}Cl_x$/**spiro-OMeTAD**/Au). The contents in parentheses are the highest efficiencies and the corresponding device architectures based on different porous structures reported so far. At present, bl-TiO_2/mp-TiO_2/perovskite/HTM-based MMOPSC and bl-TiO_2/mp-Al_2O_3/perovskite/HTM-based MSSC are the most widely studied two type device architectures. Optimization of following factors, including, (a) "scaffold" thickness and porosity modification, (b) interface/electrode engineering, (c) doping, and (d) HTM adjustment can effectively improve the device performance. Also, exploring on some new type "scaffold" substances is still necessary (e.g. MO_3[203], Zn_2SnO_4[204], $SrTiO_3$[205]). However, for fabricating these porous scaffolds as well as the thin blocking layer, especially employed in state-of-the-art perovskite solar cells, sintering process at high temperature is always needed, which increases production cost and energy consumption, and also limits the possibility of fabricating large-area, flexible devices. Thus, for a period in the future, developing low-temperature fabricated devices would be a promising direction and trend.

For PHJPSC, two configurations including a positive or inverted structure, in which a *n*-type (e.g. TiO_2 and ZnO) or *p*-type conductor (e.g. PETDOT:PSS, NiO, CuSCN, graphene oxide and polythiophene) was coated on a conductive glass, have been widely studied with the highest PCEs of 19.3% (ITO/PEIE/bl-TiO_2(Y)/ $MAPbI_{3-x}Cl_x$ /**spiro-OMeTAD**/Au) and 16.31% (ITO/PEDOT:PSS/$MAPbI_3$/**PC70BM**/Ca/Al), respectively. Apart from the above-mentioned optimization methods of (b), (c) and (d) for MMOPSC and/or MSSC, the PHJ device performance is more dependent on the perovskite morphology, in particular the film thickness, roughness, and coverage. Also, due to the similar device architecture of the inverted planar perovskite solar cells (typically devices based on a ITO/PEDOT:PSS substrate) and the OPVs, some device engineering methods for OPVs can be reference to this inverted perovskite device for further improving the device performance.

Although great success in photovoltaic field has been achieved for organometal halide perovskites, the extremely high sensitivity of organometal halide perovskites to elevated temperature and moisture is still the main limiting factor for further practical application. Also, the low reproducibility, high deviation of the device performance and environmental pollution are problems exigent to be solved. Optimizing the perovskite material and structure of devices (e.g. large-

area/flexible/durable/semitransparent/tandem device) will benefit its real application finally.[26,206-214] We believe that, in the near future, the development of perovskite solar cells will open a new chapter on solving the problem of energy crisis.

Notes and references

Shaowei Shi received a BS degree at Beijing University of Chemical Technology in 2010. Now he is a Ph.D. student in Prof. Haiqiao Wang's group, at the State Key Laboratory of Organic–Inorganic Composites, Beijing University of Chemical Technology. His research interests include the synthesis of organic semiconducting materials, and their application in electronic devices.

Dr. Yongfang Li is a professor in Institute of Chemistry, Chinese Academy of Sciences (ICCAS) since 1993, a professor in College of Chemistry, Chemical Engineering and Materials Science, Soochow University since 2012, and a Member of Chinese Academy of Sciences since 2013. He obtained his M.Sc in Chemistry from Eastern China University of Science and Technology in 1982, and his Ph.D in physical chemistry from Fudan University in 1986. His major research areas include electrochemistry of conducting polymers, and photovoltaic materials and devices for polymer solar cells. He has published more than 490 papers, and the published papers have been cited by others for more than 15000 times with an H-index of 64.

Prof. Xiaoyu Li received his B.S. in the Chemistry Department, Shandong University (1981), and his M.Sc. in the Department of Polymer Science, Beijing University of Chemical Technology (1985), and his Ph.D. in College of Materials Science and Engineering, Beijing University of Chemical Technology (1998). He is currently a Professor of State Key Laboratory of Organic–Inorganic Composites, Head of Department of Organic Functional Materials, Beijing University of Chemical Technology. His research areas involve emulsion polymerization theory, synthesis and application of water-based paint, adhesive and ink materials, and new type photoelectric functional materials.

Prof. Haiqiao Wang received his B.S. (1983), and M.Sc. (1989) in the Department of Chemistry, Huazhong University of Science and Technology, and his Ph.D. (1998) in the Department of Photoelectric Engineering, Huazhong University of Science and Technology. After postdoctoral work at Tsinghua University (1999–2001), he joined Beijing University of Chemical Technology. He is currently a Professor of the State Key Laboratory of Organic–Inorganic Composites, Beijing University of Chemical Technology. His research areas involve materials and devices of organic light emitting diode, polymer solar cells and organic field-effect transistors, and synthesis and application of water-based polymers.

[a] *State Key Laboratory of Organic-Inorganic Composites, Beijing University of Chemical Technology, Beijing 100029, China. Email: wanghaiqiao@mail.buct.edu.cn; lixy@mail.buct.edu.cn*

[b] *Beijing Engineering Research Center for the Synthesis and Applications of Waterborne Polymers, Beijing University of Chemical Technology, Beijing 100029, China*

[c] *CAS Key Laboratory of Organic Solids, Institute of Chemistry, Chinese Academy of Sciences, Beijing 100190, China*

(1) http://news.sciencemag.org/breakthrough-of-the-year-2013
(2) http://www.nature.com/news/365-days-nature-s-10-1.14367
(3) Kamat, P. V. *J. Am. Chem. Soc.* 2014, **136**, 3713.
(4) Cheng, Z.; Lin, J. *CrystEngComm.* 2010, **12**, 2646.
(5) Li, C.; Lu, X.; Ding, W.; Feng, L.; Gao, Y.; Guo, Z. *Acta Crystallogr., Sect. B: Struct. Sci* 2008, **64**, 702.
(6) Green, M. A.; Ho-Baillie, A.; Snaith, H. J. *Nat. Photonics* 2014, **8**, 506.
(7) Borriello, I.; Cantele, G.; Ninno, D. *Phys. Rev. B* 2008, **77**, 235214
(8) O'Regan, B.; Grätzel, M. *Nature* 1991, **353**, 737
(9) Yella, A.; Lee, H. W.; Tsao, H. N.; Yi, C.; Chandiran, A. K.; Nazeeruddin, M. K.; Diau, E. W.; Yeh, C. Y.; Zakeeruddin, S. M.; Grätzel, M. *Science* 2011, **334**, 629.
(10) Bach, U.; Lupo, D.; Comte, P.; Moser, J. E.; Weissörtel, F.;Salbeck, J.; Spreitzer, H.; Grätzel, M. *Nature* 1998, **395**, 583.
(11) Burschka, J.; Dualeh, A.; Kessler, F.; Baranoff, E.; Cevey-Ha, N. L.; Yi, C.; Nazeeruddin, M. K.; Grätzel, M. *J. Am. Chem. Soc.* 2011, **133**, 18042.
(12) Kim, H. S.; Lee, C. R.; Im, J. H.; Lee, K. B.; Moehl, T.; Marchioro, A.; Moon, S. J.; Humphry-Baker, R.; Yum, J. H.; Moser, J. E.; Grätzel, M.; Park, N. G. *Sci. Rep.* 2012, **2**, 591.

(13) Lee, M. M.; Teuscher, J.; Miyasaka, T.; Murakami, T. N.; Snaith, H. J. *Science* 2012, **338**, 643.
(14) Etgar, L.; Gao, P.; Xue, Z.; Peng, Q.; Chandiran, A. K.; Liu, B.; Nazeeruddin, M. K.; Grätzel, M. *J. Am. Chem. Soc.* 2012, **134**, 17396.
(15) Kojima, A.; Teshima, K.; Shirai, Y.; Miyasaka, T. *J. Am. Chem. Soc.* 2009, **131**, 6050.
(16) Im, J. H.; Lee, C. R.; Lee, J. W.; Park, S. W.; Park, N. G. *Nanoscale* 2011, **3**, 4088.
(17) Im, J. H.; Chung, J.; Kim, S. J.; Park, N. G. *Nanoscale Res. Lett.* 2012, **7**, 353
(18) Burschka, J.; Pellet, N.; Moon, S. J.; Humphry-Baker, R.; Gao, P.; Nazeeruddin, M. K.; Grätzel, M. *Nature* 2013, **499**, 316.
(19) Liu, M.; Johnston, M. B.; Snaith, H. J. *Nature* 2013, **501**, 395.
(20) Heo, J. H.; Im, S. H.; Noh, J. H.; Mandal, T. N.; Lim, C.-S.; Chang, J. A.; Lee, Y. H.; Kim, H.-j.; Sarkar, A.; Nazeeruddin, M. K.; Grätzel, M.; Seok, S. I. *Nat. Photonics* 2013, **7**, 486.
(21) Im, J. H.; Jang, I. H.; Pellet, N.; Grätzel, M.; Park, N. G. *Nat. Nanotech.* 2014, **9**, 927.
(22) Wojciechowski, K.; Saliba, M.; Leijtens, T.; Abate, A.; Snaith, H. J. *Energy. Environ. Sci.* 2014, **7**, 1142.
(23) Zhou, H.; Chen, Q.; Li, G.; Luo, S.; Song, T. B.; Duan, H. S.; Hong, Z.; You, J.; Liu, Y.; Yang, Y. *Science* 2014, **345**, 542.
(24) Jeon, N. J.; Noh, J. H.; Kim, Y. C.; Yang, W. S.; Ryu, S.; Seok, S. I. *Nat. Mater.* 2014, **13**, 897.
(25) Kim, H. B.; Choi, H.; Jeong, J.; Kim, S.; Walker, B.; Song, S.; Kim, J. Y. *Nanoscale* 2014, **6**, 6679.
(26) Seo, J.; Park, S.; Chan Kim, Y.; Jeon, N. J.; Noh, J. H.; Yoon, S. C.; Seok, S. I. *Energy. Environ. Sci.* 2014, **7**, 2642.
(27) Xiao, M.; Huang, F.; Huang, W.; Dkhissi, Y.; Zhu, Y.; Etheridge, J.; Gray-Weale, A.; Bach, U.; Cheng, Y. B.; Spiccia, L. *Angew. Chem. Int. Ed.* 2014, **53**, 9898.
(28) Paek, S.; Cho, N.; Choi, H.; Jeong, H.; Lim, J. S.; Hwang, J.-Y.; Lee, J. K.; Ko, J. *J. Phys. Chem. C* 2014, **118**, 25899.
(29) Jung, J. W.; Williams, S. T.; Jen, A. K. Y. *RSC Adv.* 2014, **4**, 62971.
(30) Kang, R.; Kim, J.-E.; Yeo, J.-S.; Lee, S.; Jeon, Y.-J.; Kim, D.-Y. *J. Phys. Chem. C* 2014, **118**, 26513.
(31) Eperon, G. E.; Burlakov, V. M.; Docampo, P.; Goriely, A.; Snaith, H. J. *Adv. Funct. Mater.* 2014, **24**, 151.
(32) Hsu, H. L.; Chen, C. P.; Chang, J. Y.; Yu, Y. Y.; Shen, Y. K. *Nanoscale* 2014, **6**, 10281.
(33) Saliba, M.; Tan, K. W.; Sai, H.; Moore, D. T.; Scott, T.; Zhang, W.; Estroff, L. A.; Wiesner, U.; Snaith, H. J. *J. Phys. Chem. C* 2014, **118**, 17171.
(34) Dualeh, A.; Tétreault, N.; Moehl, T.; Gao, P.; Nazeeruddin, M. K.; Grätzel, M. *Adv. Funct. Mater.* 2014, **24**, 3250.
(35) Liang, P. W.; Liao, C. Y.; Chueh, C. C.; Zuo, F.; Williams, S. T.; Xin, X. K.; Lin, J.; Jen, A. K. *Adv. Mater.* 2014, **26**, 3748.
(36) Zhao, Y.; Zhu, K. *J. Phys. Chem. C* 2014, **118**, 9412.
(37) Zhao, Y.; Zhu, K. *J. Am. Chem. Soc.* 2014, **136**, 12241.
(38) Zuo, C.; Ding, L. *Nanoscale* 2014, **6**, 9935.
(39) Kangning Liang, D. B. M., * and Michael T. Prikas *Chem. Mater*. 1998, **10**, 403
(40) Ma, Y.; Zheng, L.; Chung, Y.-H.; Chu, S.; Xiao, L.; Chen, Z.; Wang, S.; Qu, B.; Gong, Q.; Wu, Z.; Hou, X. *Chem. Commun.*2014, **50**, 12458.
(41) Wu, Y.; Islam, A.; Yang, X.; Qin, C.; Liu, J.; Zhang, K.; Peng, W.; Han, L. *Energy. Environ. Sci.* 2014, **7**, 2934.
(42) Shi, J.; Luo, Y.; Wei, H.; Luo, J.; Dong, J.; Lv, S.; Xiao, J.; Xu, Y.; Zhu, L.; Xu, X.; Wu, H.; Li, D.; Meng, Q. *ACS Appl. Mater. Interfaces* 2014, **6**, 9711.
(43) Docampo, P.; Hanusch, F. C.; Giesbrecht, N.; Angloher, P.; Ivanova, A.; Bein, T. *APL Mat.* 2014, **2**, 081508.
(44) Zheng, L.; Ma, Y.; Chu, S.; Wang, S.; Qu, B.; Xiao, L.; Chen, Z.; Gong, Q.; Wu, Z.; Hou, X. *Nanoscale* 2014, **6**, 8171.
(45) Cao, D. H.; Stoumpos, C. C.; Malliakas, C. D.; Katz, M. J.; Farha, O. K.; Hupp, J. T.; Kanatzidis, M. G. *APL Mat.* 2014, **2**, 091101.
(46) Bi, D.; Moon, S.-J.; Häggman, L.; Boschloo, G.; Yang, L.; Johansson, E. M. J.; Nazeeruddin, M. K.; Grätzel, M.; Hagfeldt, A. *RSC Adv.* 2013, **3**, 18762.
(47) Liu, D.; Kelly, T. L. *Nat. Photonics* 2013, **8**, 133.
(48) Chen, Q.; Zhou, H.; Hong, Z.; Luo, S.; Duan, H. S.; Wang, H. H.; Liu, Y.; Li, G.; Yang, Y. *J. Am. Chem. Soc.* 2014, **136**, 622.
(49) Xiao, Z.; Bi, C.; Shao, Y.; Dong, Q.; Wang, Q.; Yuan, Y.; Wang, C.; Gao, Y.; Huang, J. *Energy. Environ. Sci.* 2014, **7**, 2619
(50) Chiang, C.-H.; Tseng, Z.-L.; Wu, C.-G. *J. Mater. Chem. A* 2014, **2**, 15897.
(51) Im, J.-H.; Kim, H.-S.; Park, N.-G. *APL Mat.* 2014, **2**, 081510.
(52) Barrows, A. T.; Pearson, A. J.; Kwak, C. K.; Dunbar, A. D. F.; Buckley, A. R.; Lidzey, D. G. *Energy. Environ. Sci.* 2014, **7**, 2944.
(53) Moore, D. T.; Sai, H.; Wee Tan, K.; Estroff, L. A.; Wiesner, U. *APL Mat.* 2014, **2**, 081802.
(54) Cohen, B.-E.; Gamliel, S.; Etgar, L. *APL Mat.* 2014, **2**, 081502.
(55) Hu, H.; Wang, D.; Zhou, Y.; Zhang, J.; Lv, S.; Pang, S.; Chen, X.; Liu, Z.; Padture, N. P.; Cui, G. *RSC Adv.* 2014, **4**, 28964.
(56) Chen, C. W.; Kang, H. W.; Hsiao, S. Y.; Yang, P. F.; Chiang, K. M.; Lin, H. W. *Adv. Mater.* 2014, **26**, 6647.
(57) Chen, Q.; Zhou, H.; Song, T. B.; Luo, S.; Hong, Z.; Duan, H. S.; Dou, L.; Liu, Y.; Yang, Y. *Nano Lett.* 2014, **14**, 4158.
(58) Supasai, T.; Rujisamphan, N.; Ullrich, K.; Chemseddine, A.; Dittrich, T. *Appl. Phys. Lett.* 2013, **103**, 183906.
(59) Wang, L.; McCleese, C.; Kovalsky, A.; Zhao, Y.; Burda, C. *J. Am. Chem. Soc.* 2014, **136**, 12205.
(60) Jeon, N. J.; Lee, H. G.; Kim, Y. C.; Seo, J.; Noh, J. H.; Lee, J.; Seok, S. I. *J. Am. Chem. Soc.* 2014, **136**, 7837.
(61) Bai, Y.; Mora-Sero, I.; De Angelis, F.; Bisquert, J.; Wang, P. *Chem. Rev.* 2014, **114**, 10095.
(62) Murugadoss, G.; Mizuta, G.; Tanaka, S.; Nishino, H.; Umeyama, T.; Imahori, H.; Ito, S. *APL Mat.* 2014, **2**, 081511.
(63) Conings, B.; Baeten, L.; Jacobs, T.; Dera, R.; D'Haen, J.; Manca, J.; Boyen, H. G. *APL Mat.* 2014, **2**, 081505.
(64) Conings, B.; Baeten, L.; De Dobbelaere, C.; D'Haen, J.; Manca, J.; Boyen, H. G. *Adv. Mater.* 2014, **26**, 2041.
(65) Liu, W.; Zhang, Y. *J. Mater. Chem. A* 2014, **2**, 10244.
(66) Yella, A.; Heiniger, L. P.; Gao, P.; Nazeeruddin, M. K.; Grätzel, M. *Nano Lett.* 2014, **14**, 2591.

(67) Ball, J. M.; Lee, M. M.; Hey, A.; Snaith, H. J. *Energy. Environ. Sci.* 2013, **6**, 1739.
(68) Wu, Y.; Yang, X.; Chen, H.; Zhang, K.; Qin, C.; Liu, J.; Peng, W.; Islam, A.; Bi, E.; Ye, F.; Yin, M.; Zhang, P.; Han, L. *Appl. Phys. Express* 2014, **7**, 052301.
(69) Chandiran, A. K.; Yella, A.; Mayer, M. T.; Gao, P.; Nazeeruddin, M. K.; Grätzel, M. *Adv. Mater.* 2014, **26**, 4309.
(70) Qin, P.; Domanski, A. L.; Chandiran, A. K.; Berger, R.; Butt, H. J.; Dar, M. I.; Moehl, T.; Tetreault, N.; Gao, P.; Ahmad, S.; Nazeeruddin, M. K.; Grätzel, M. *Nanoscale* 2014, **6**, 1508.
(71) Xia, J.; Masaki, N.; Jiang, K.; Yanagida, S. *J. Phys. Chem. B* 2006, **110**, 25222
(72) Ke, W.; Fang, G.; Wang, J.; Qin, P.; Tao, H.; Lei, H.; Liu, Q.; Dai, X.; Zhao, X. *ACS Appl. Mater. Interfaces* 2014, **6**, 15959.
(73) Choi, J. J.; Yang, X.; Norman, Z. M.; Billinge, S. J.; Owen, J. S. *Nano Lett.* 2014, **14**, 127.
(74) Edri, E.; Kirmayer, S.; Henning, A.; Mukhopadhyay, S.; Gartsman, K.; Rosenwaks, Y.; Hodes, G.; Cahen, D. *Nano Lett.* 2014, **14**, 1000.
(75) Shen, Q.; Ogomi, Y.; Chang, J.; Tsukamoto, S.; Kukihara, K.; Oshima, T.; Osada, N.; Yoshino, K.; Katayama, K.; Toyoda, T.; Hayase, S. *Phys. Chem. Chem. Phys.* 2014, **16**, 19984.
(76) Zhao, Y.; Nardes, A. M.; Zhu, K. *Faraday Discuss.*2014. **DOI:** 10.1039/C4FD00128A
(77) Lindblad, R.; Bi, D.; Park, B.-w.; Oscarsson, J.; Gorgoi, M.; Siegbahn, H.; Odelius, M.; Johansson, E. M. J.; Rensmo, H. *J. Phys. Chem. Lett.* 2014, **5**, 648.
(78) Lee, J. W.; Lee, T. Y.; Yoo, P. J.; Grätzel, M.; Mhaisalkar, S.; Park, N. G. *J. Mater. Chem. A* 2014, **2**, 9251.
(79) Dar, M. I.; Ramos, F. J.; Xue, Z.; Liu, B.; Ahmad, S.; Shivashankar, S. A.; Nazeeruddin, M. K.; Grätzel, M. *Chem. Mater.* 2014, **26**, 4675.
(80) Rong, Y.; Ku, Z.; Mei, A.; Liu, T.; Xu, M.; Ko, S.; Li, X.; Han, H. *J. Phys. Chem. Lett.* 2014, **5**, 2160.
(81) Kim, H. S.; Lee, J. W.; Yantara, N.; Boix, P. P.; Kulkarni, S. A.; Mhaisalkar, S.; Grätzel, M.; Park, N. G. *Nano Lett.* 2013, **13**, 2412.
(82) Manseki, K.; Ikeya, T.; Tamura, A.; Ban, T.; Sugiura, T.; Yoshida, T. *RSC Adv.* 2014, **4**, 9652.
(83) Qiu, J.; Qiu, Y.; Yan, K.; Zhong, M.; Mu, C.; Yan, H.; Yang, S. *Nanoscale* 2013, **5**, 3245.
(84) Chen, H.; Wei, Z.; Yan, K.; Yi, Y.; Wang, J.; Yang, S. *Faraday Discuss.*2014. **DOI:** 10.1039/C4FD00155A
(85) Yang, M.; Guo, R.; Kadel, K.; Liu, Y.; O'Shea, K.; Bone, R.; Wang, X.; He, J.; Li, W. *J. Mater. Chem. A* 2014, **2**, 19616.
(86) Gao, X.; Li, J.; Baker, J.; Hou, Y.; Guan, D.; Chen, J.; Yuan, C. *Chem. Commun.*2014, **50**, 6368.
(87) Xiao, Y. M.; Han, G. Y.; Li, Y. P.; Li, M. Y.; Wu, J. H. *J. Mater. Chem. A* 2014, **2**, 16856.
(88) Dharani, S.; Mulmudi, H. K.; Yantara, N.; Thu Trang, P. T.; Park, N. G.; Graetzel, M.; Mhaisalkar, S.; Mathews, N.; Boix, P. P. *Nanoscale* 2014, **6**, 1675.
(89) Jiang, Q.; Sheng, X.; Li, Y.; Feng, X.; Xu, T. *Chem. Commun.*2014, **50**, 14720.
(90) Crossland, E. J.; Noel, N.; Sivaram, V.; Leijtens, T.; Alexander-Webber, J. A.; Snaith, H. J. *Nature* 2013, **495**, 215.
(91) Han, G. S.; Lee, S.; Noh, J. H.; Chung, H. S.; Park, J. H.; Swain, B. S.; Im, J. H.; Park, N. G.; Jung, H. S. *Nanoscale* 2014, **6**, 6127.
(92) Zhang, Q.; Dandeneau, C. S.; Zhou, X.; Cao, G. *Adv. Mater.* 2009, **21**, 4087.
(93) Anta, J. A.; Guillén, E.; Tena-Zaera, R. *J. Phys. Chem. C* 2012, **116**, 11413.
(94) Bi, D.; Boschloo, G.; Schwarzmuller, S.; Yang, L.; Johansson, E. M.; Hagfeldt, A. *Nanoscale* 2013, **5**, 11686.
(95) Son, D. Y.; Im, J. H.; Kim, H. S.; Park, N. G. *J Phys Chem C* 2014, **118**, 16567.
(96) Kumar, M. H.; Yantara, N.; Dharani, S.; Graetzel, M.; Mhaisalkar, S.; Boix, P. P.; Mathews, N. *Chem. Commun.*2013, **49**, 11089.
(97) Ramos, F. J.; Lopez-Santos, M. C.; Guillen, E.; Nazeeruddin, M. K.; Grätzel, M.; Gonzalez-Elipe, A. R.; Ahmad, S. *ChemPhysChem* 2014, **15**, 1148.
(98) Mahmood, K.; Swain, B. S.; Jung, H. S. *Nanoscale* 2014, **6**, 9127.
(99) Mahmood, K.; Munir, R.; Swain, B. S.; Han, G.-S.; Kim, B.-J.; Jung, H. S. *RSC Adv.* 2014, **4**, 9072.
(100) Dong, J.; Zhao, Y.; Shi, J.; Wei, H.; Xiao, J.; Xu, X.; Luo, J.; Xu, J.; Li, D.; Luo, Y.; Meng, Q. *Chem. Commun.*2014, **50**, 13381.
(101) Wang, K. C.; Jeng, J. Y.; Shen, P. S.; Chang, Y. C.; Diau, E. W. G.; Tsai, C. H.; Chao, T. Y.; Hsu, H. C.; Lin, P. Y.; Chen, P.; Guo, T. F.; Wen, T. C. *Sci. Rep.* 2014, **4**, 4756.
(102) Jeng, J.-Y.; Chen, K.-C.; Chiang, T.-Y.; Lin, P.-Y.; Tsai, T.-D.; Chang, Y.-C.; Guo, T.-F.; Chen, P.; Wen, T.-C.; Hsu, Y.-J. *Adv. Mater.* 2014, **26**, 4107.
(103) Hu, L.; Peng, J.; Wang, W.; Xia, Z.; Yuan, J.; Lu, J.; Huang, X.; Ma, W.; Song, H.; Chen, W.; Cheng, Y.-B.; Tang, J. *ACS Photonics* 2014, **1**, 547.
(104) Wang, K. C.; Shen, P. S.; Li, M. H.; Chen, S.; Lin, M. W.; Chen, P.; Guo, T. F. *ACS Appl. Mater. Interfaces* 2014, **6**, 11851.
(105) Edri, E.; Kirmayer, S.; Cahen, D.; Hodes, G. *J. Phys. Chem. Lett.* 2013, **4**, 897.
(106) Zhang, W.; Saliba, M.; Stranks, S. D.; Sun, Y.; Shi, X.; Wiesner, U.; Snaith, H. J. *Nano Lett.* 2013, **13**, 4505.
(107) Carnie, M. J.; Charbonneau, C.; Davies, M. L.; Troughton, J.; Watson, T. M.; Wojciechowski, K.; Snaith, H.; Worsley, D. A. *Chem. Commun.*2013, **49**, 7893.
(108) Abate, A.; Saliba, M.; Hollman, D. J.; Stranks, S. D.; Wojciechowski, K.; Avolio, R.; Grancini, G.; Petrozza, A.; Snaith, H. J. *Nano Lett.* 2014, **14**, 3247.
(109) Pathak, S. K.; Abate, A.; Ruckdeschel, P.; Roose, B.; Godel, K. C.; Vaynzof, Y.; Santhala, A.; Watanabe, S. I.; Hollman, D. J.; Noel, N.; Sepe, A.; Wiesner, U.; Friend, R.; Snaith, H. J.; Steiner, U. *Adv. Funct. Mater.* 2014, **24**, 6046.
(110) Habisreutinger, S. N.; Leijtens, T.; Eperon, G. E.; Stranks, S. D.; Nicholas, R. J.; Snaith, H. J. *Nano Lett.* 2014, **14**, 5561.
(111) Wang, J. T.; Ball, J. M.; Barea, E. M.; Abate, A.; Alexander-Webber, J. A.; Huang, J.; Saliba, M.; Mora-Sero, I.; Bisquert, J.; Snaith, H. J.; Nicholas, R. J. *Nano Lett.* 2014, **14**, 724.
(112) Dong, X.; Hu, H.; Lin, B.; Ding, J.; Yuan, N. *Chem. Commun.* 2014, **50**, 14405.

(113) Kim, H. S.; Mora-Sero, I.; Gonzalez-Pedro, V.; Fabregat-Santiago, F.; Juarez-Perez, E. J.; Park, N. G.; Bisquert, J. *Nat. Commun.*2013, **4**, 2242.
(114) Hwang, S. H.; Roh, J.; Lee, J.; Ryu, J.; Yun, J.; Jang, J. *J. Mater. Chem. A* 2014, **2**, 16429.
(115) Stranks, S. D.; Eperon, G. E.; Grancini, G.; Menelaou, C.; Alcocer, M. J.; Leijtens, T.; Herz, L. M.; Petrozza, A.; Snaith, H. J. *Science* 2013, **342**, 341.
(116) Xing, G.; Mathews, N.; Sun, S.; Lim, S. S.; Lam, Y. M.; Grätzel, M.; Mhaisalkar, S.; Sum, T. C. *Science* 2013, **342**, 344.
(117) Docampo, P.; Hanusch, F. C.; Stranks, S. D.; Döblinger, M.; Feckl, J. M.; Ehrensperger, M.; Minar, N. K.; Johnston, M. B.; Snaith, H. J.; Bein, T. *Adv. Energy Mater.* 2014, **4**, DOI: 10.1002/aenm.201400355
(118) Kim, J.; Kim, G.; Kim, T. K.; Kwon, S.; Back, H.; Lee, J.; Lee, S. H.; Kang, H.; Lee, K. *J. Mater. Chem. A* 2014, **2**, 17291.
(119) Liang, L.; Huang, Z.; Cai, L.; Chen, W.; Wang, B.; Chen, K.; Bai, H.; Tian, Q.; Fan, B. *ACS Appl. Mater. Interfaces* 2014, **6**, 20585.
(120) Zheng, L.; Chung, Y. H.; Ma, Y.; Zhang, L.; Xiao, L.; Chen, Z.; Wang, S.; Qu, B.; Gong, Q. *Chem. Commun.*2014, **50**, 11196.
(121) Chavhan, S.; Miguel, O.; Grande, H. J.; Gonzalez-Pedro, V.; Sanchez, R. S.; Barea, E. M.; Mora-Sero, I.; Tena-Zaera, R. *J. Mater. Chem. A* 2014, **2**, 12754.
(122) Noel, N. K.; Abate, A.; Stranks, S. D.; Parrott, E. S.; Burlakov, V. M.; Goriely, A.; Snaith, H. J. *ACS Nano*, 2014, **8**, 9815
(123) Jeng, J. Y.; Chiang, Y. F.; Lee, M. H.; Peng, S. R.; Guo, T. F.; Chen, P.; Wen, T. C. *Adv. Mater.* 2013, **25**, 3727.
(124) Sun, S.; Salim, T.; Mathews, N.; Duchamp, M.; Boothroyd, C.; Xing, G.; Sum, T. C.; Lam, Y. M. *Energy. Environ. Sci.* 2014, **7**, 399.
(125) Docampo, P.; Ball, J. M.; Darwich, M.; Eperon, G. E.; Snaith, H. J. *Nat. Commun.*2013, **4**, 2761.
(126) Malinkiewicz, O.; Yella, A.; Lee, Y. H.; Espallargas, G. M.; Graetzel, M.; Nazeeruddin, M. K.; Bolink, H. J. *Nat. Photonics* 2013, **8**, 128.
(127) Malinkiewicz, O.; Roldán-Carmona, C.; Soriano, A.; Bandiello, E.; Camacho, L.; Nazeeruddin, M. K.; Bolink, H. J. *Adv. Energy Mater.* 2014, **4**, DOI: 10.1002/aenm.201400345
(128) You, J.; Hong, Z.; Yang, Y. M.; Chen, Q.; Cai, M.; Song, T. B.; Chen, C. C.; Lu, S.; Liu, Y.; Zhou, H.; Yang, Y. *ACS nano* 2014, **8**, 1674.
(129) Lim, K.-G.; Kim, H.-B.; Jeong, J.; Kim, H.; Kim, J. Y.; Lee, T.-W. *Adv. Mater.* 2014, **26**, 6461.
(130) Wang, Q.; Shao, Y. C.; Dong, Q. F.; Xiao, Z. G.; Yuan, Y. B.; Huang, J. S. *Energy. Environ. Sci.* 2014, **7**, 2359.
(131) Xiao, Z.; Dong, Q.; Bi, C.; Shao, Y.; Yuan, Y.; Huang, J. *Adv. Mater.* 2014, **26**, 6503.
(132) Subbiah, A. S.; Halder, A.; Ghosh, S.; Mahuli, N.; Hodes, G.; Sarkar, S. K. *J. Phys. Chem. Lett.* 2014, **5**, 1748.
(133) Zhu, Z.; Bai, Y.; Zhang, T.; Liu, Z.; Long, X.; Wei, Z.; Wang, Z.; Zhang, L.; Wang, J.; Yan, F.; Yang, S. *Angew. Chem. Int. Ed.* 2014, **53**, 12571.
(134) Wu, Z.; Bai, S.; Xiang, J.; Yuan, Z.; Yang, Y.; Cui, W.; Gao, X.; Liu, Z.; Jin, Y.; Sun, B. *Nanoscale* 2014, **6**, 10505.
(135) Yan, W.; Li, Y.; Sun, W.; Peng, H.; Ye, S.; Liu, Z.; Bian, Z.; Huang, C. *RSC Adv.* 2014, **4**, 33039.
(136) Bi, D.; Yang, L.; Boschloo, G.; Hagfeldt, A.; Johansson, E. M. J. *J. Phys. Chem. Lett.* 2013, **4**, 1532.
(137) Jeon, N. J.; Lee, J.; Noh, J. H.; Nazeeruddin, M. K.; Grätzel, M.; Seok, S. I. *J. Am. Chem. Soc.* 2013, **135**, 19087.
(138) Li, H.; Fu, K.; Hagfeldt, A.; Grätzel, M.; Mhaisalkar, S. G.; Grimsdale, A. C. *Angew. Chem. Int. Ed.* 2014, **53**, 4085.
(139) Krishnamoorthy, T.; Kunwu, F.; Boix, P. P.; Li, H.; Koh, T. M.; Leong, W. L.; Powar, S.; Grimsdale, A.; Grätzel, M.; Mathews, N.; Mhaisalkar, S. G. *J. Mater. Chem. A* 2014, **2**, 6305.
(140) Krishna, A.; Sabba, D.; Li, H. R.; Yin, J.; Boix, P. P.; Soci, C.; Mhaisalkar, S. G.; Grimsdale, A. C. *Chemical Science* 2014, **5**, 2702.
(141) Choi, H.; Paek, S.; Lim, N.; Lee, Y. H.; Nazeeruddin, M. K.; Ko, J. *Chem. – Eur. J.* 2014, **20**, 10894.
(142) Song, Y.; Lv, S.; Liu, X.; Li, X.; Wang, S.; Wei, H.; Li, D.; Xiao, Y.; Meng, Q. *Chem. Commun.* 2014, **50**, 15239.
(143) Xu, B.; Sheibani, E.; Liu, P.; Zhang, J.; Tian, H.; Vlachopoulos, N.; Boschloo, G.; Kloo, L.; Hagfeldt, A.; Sun, L. *Adv. Mater.* 2014, **26**, 6629.
(144) Sung, S. D.; Kang, M. S.; Choi, I. T.; Kim, H. M.; Kim, H.; Hong, M.; Kim, H. K.; Lee, W. I. *Chem. Commun.*2014, **50**, 14161.
(145) Wang, J.; Wang, S.; Li, X.; Zhu, L.; Meng, Q.; Xiao, Y.; Li, D. *Chem. Commun.*2014, **50**, 5829.
(146) Lv, S.; Han, L.; Xiao, J.; Zhu, L.; Shi, J.; Wei, H.; Xu, Y.; Dong, J.; Xu, X.; Li, D.; Wang, S.; Luo, Y.; Meng, Q.; Li, X. *Chem. Commun.*2014, **50**, 6931.
(147) Xiao, J.; Han, L.; Zhu, L.; Lv, S.; Shi, J.; Wei, H.; Xu, Y.; Dong, J.; Xu, X.; Xiao, Y.; Li, D.; Wang, S.; Luo, Y.; Li, X.; Meng, Q. *RSC Adv.* 2014, **4**, 32918.
(148) Polander, L. E.; Pahner, P.; Schwarze, M.; Saalfrank, M.; Koerner, C.; Leo, K. *APL Mat.* 2014, **2**, 081503.
(149) Edri, E.; Kirmayer, S.; Kulbak, M.; Hodes, G.; Cahen, D. *J. Phys. Chem. Lett.* 2014, **5**, 429.
(150) Qin, P.; Kast, H.; Nazeeruddin, M. K.; Zakeeruddin, S. M.; Mishra, A.; Bäuerle, P.; Grätzel, M. *Energy. Environ. Sci.* 2014, **7**, 2981.
(151) Qin, P.; Paek, S.; Dar, M. I.; Pellet, N.; Ko, J.; Grätzel, M.; Nazeeruddin, M. K. *J. Am. Chem. Soc.* 2014, **136**, 8516.
(152) Liu, J.; Wu, Y.; Qin, C.; Yang, X.; Yasuda, T.; Islam, A.; Zhang, K.; Peng, W.; Chen, W.; Han, L. *Energy. Environ. Sci.* 2014, **7**, 2963.
(153) Cai, B.; Xing, Y.; Yang, Z.; Zhang, W.-H.; Qiu, J. *Energy. Environ. Sci.* 2013, **6**, 1480.
(154) Di Giacomo, F.; Razza, S.; Matteocci, F.; D'Epifanio, A.; Licoccia, S.; Brown, T. M.; Di Carlo, A. *J. Power Sources* 2014, **251**, 152.
(155) Guo, Y.; Liu, C.; Lnoue, K.; Harano, K.; Tanaka, H.; Nakamura, E. *J. Mater. Chem. A* 2014, **2**, 13827.
(156) Heo, J. H.; Im, S. H. *Phys. Status solidi -R* 2014, **8**, 816.
(157) Zhang, M.; Lyu, M.; Yu, H.; Yun, J.-H.; Wang, Q.; Wang, L. *Chem. – Eur. J.* 2014, **21**, 434..
(158) Ryu, S.; Noh, J. H.; Jeon, N. J.; Kim, Y. C.; Yang, S.; Seo, J. W.; Seok, S. I. *Energy. Environ. Sci.* 2014, **7**, 2614.
(159) Zhu, Z.; Bai, Y.; Lee, H. K. H.; Mu, C.; Zhang, T.; Zhang, L.; Wang, J.; Yan, H.; So, S. K.; Yang, S. *Adv. Funct. Mater.* 2014, **24**, 7357.

(160) Qin, P.; Tetreault, N.; Dar, M. I.; Gao, P.; McCall, K. L.; Rutter, S. R.; Ogier, S. D.; Forrest, N. D.; Bissett, J. S.; Simms, M. J.; Page, A. J.; Fisher, R.; Grätzel, M.; Nazeeruddin, M. K. *Adv. Energy Mater.* 2014, DOI: 10.1002/aenm.201400980
(161) Kwon, Y. S.; Lim, J.; Yun, H.-J.; Kim, Y.-H.; Park, T. *Energy. Environ. Sci.* 2014, **7**, 1454.
(162) Lee, J. W.; Park, S.; Ko, M. J.; Son, H. J.; Park, N. G. *ChemPhysChem* 2014, **15**, 2595.
(163) Abrusci, A.; Stranks, S. D.; Docampo, P.; Yip, H. L.; Jen, A. K.; Snaith, H. J. *Nano Lett.* 2013, **13**, 3124.
(164) Christians, J. A.; Fung, R. C.; Kamat, P. V. *J. Am. Chem. Soc.* 2014, **136**, 758.
(165) Ito, S.; Tanaka, S.; Manabe, K.; Nishino, H. *J. Phys. Chem. C* 2014, **118**, 16995.
(166) Ito, S.; Tanaka, S.; Vahlman, H.; Nishino, H.; Manabe, K.; Lund, P. *ChemPhysChem* 2014, **15**, 1194.
(167) Qin, P.; Tanaka, S.; Ito, S.; Tetreault, N.; Manabe, K.; Nishino, H.; Nazeeruddin, M. K.; Grätzel, M. *Nat. Commun.*2014, **5**, 3834.
(168) Irwin, M. D.; Buchholz, D. B.; Hains, A. W.; Chang, R. P. H.; Marks, T. J. *PNAS* 2008, **105**, 2783.
(169) Steirer, K. X.; Ndione, P. F.; Widjonarko, N. E.; Lloyd, M. T.; Meyer, J.; Ratcliff, E. L.; Kahn, A.; Armstrong, N. R.; Curtis, C. J.; Ginley, D. S.; Berry, J. J.; Olson, D. C. *Adv. Energy Mater.* 2011, **1**, 813.
(170) Laban, W. A.; Etgar, L. *Energy. Environ. Sci.* 2013, **6**, 3249.
(171) Aharon, S.; Gamliel, S.; Cohen, B. E.; Etgar, L. *Phys. Chem. Chem. Phys.* 2014, **16**, 10512.
(172) Aharon, S.; El Cohen, B.; Etgar, L. *J. Phys. Chem. C* 2014, **118**, 17160.
(173) Shi, J. J.; Dong, W.; Xu, Y. Z.; Li, C. H.; Lv, S. T.; Zhu, L. F.; Dong, J.; Luo, Y. H.; Li, D. M.; Meng, Q. B.; Chen, Q. *Chinese Phys. Lett.* 2013, **30**, 128402.
(174) Xu, Y.; Shi, J.; Lv, S.; Zhu, L.; Dong, J.; Wu, H.; Xiao, Y.; Luo, Y.; Wang, S.; Li, D.; Li, X.; Meng, Q. *ACS Appl. Mater. Interfaces* 2014, **6**, 5651.
(175) Shi, J.; Dong, J.; Lv, S.; Xu, Y.; Zhu, L.; Xiao, J.; Xu, X.; Wu, H.; Li, D.; Luo, Y.; Meng, Q. *Appl. Phys. Lett.* 2014, **104**, 063901.
(176) Xiao, Y. M.; Han, G. Y.; Li, Y. P.; Li, M. Y.; Chang, Y. Z.; Wu, J. H. *J. Mater. Chem. A* 2014, **2**, 16531.
(177) Hao, F.; Stoumpos, C. C.; Liu, Z.; Chang, R. P.; Kanatzidis, M. G. *J. Am. Chem. Soc.* 2014, **136** , 16411.
(178) Ku, Z.; Rong, Y.; Xu, M.; Liu, T.; Han, H. *Sci. Rep.* 2013, **3**, 3132.
(179) Xu, M.; Rong, Y.; Ku, Z.; Mei, A.; Liu, T.; Zhang, L.; Li, X.; Han, H. *J. Mater. Chem. A* 2014, **2**, 8607.
(180) Hu, M.; Liu, L.; Mei, A.; Yang, Y.; Liu, T.; Han, H. *J. Mater. Chem. A* 2014, **2**, 17115.
(181) Mei, A.; Li, X.; Liu, L.; Ku, Z.; Liu, T.; Rong, Y.; Xu, M.; Hu, M.; Chen, J.; Yang, Y.; Grätzel, M.; Han, H. *Science* 2014, **345**, 295.
(182) Liu, Z.; Zhang, M.; Xu, X.; Bu, L.; Zhang, W.; Li, W.; Zhao, Z.; Wang, M.; Cheng, Y. B.; He, H. *Dalton Trans.* 2014. **DOI:** 10.1039/C4DT02904F
(183) Zhang, F.; Yang, X.; Wang, H.; Cheng, M.; Zhao, J.; Sun, L. *ACS Appl. Mater. Interfaces* 2014, **6**, 16140.
(184) Zhou, H.; Shi, Y.; Dong, Q.; Zhang, H.; Xing, Y.; Wang, K.; Du, Y.; Ma, T. *J. Phys. Chem. Lett.* 2014, **5**, 3241.
(185) Yang, Y.; Xiao, J.; Wei, H.; Zhu, L.; Li, D.; Luo, Y.; Wu, H.; Meng, Q. *RSC Adv.* 2014, **4**, 52825.
(186) Wei, Z.; Chen, H.; Yan, K.; Yang, S. *Angew. Chem. Int. Ed.* 2014, **53**, 13239.
(187) Kitazawa, N.; Watanabe, Y.; Nakamura, Y. *J .Mater. Sci.* 2002, **37**, 3585.
(188) Noh, J. H.; Im, S. H.; Heo, J. H.; Mandal, T. N.; Seok, S. I. *Nano Lett.* 2013, **13**, 1764.
(189) Koh, T. M.; Fu, K.; Fang, Y.; Chen, S.; Sum, T. C.; Mathews, N.; Mhaisalkar, S. G.; Boix, P. P.; Baikie, T. *J. Phys. Chem. C* 2014, **118**, 16458.
(190) Pang, S.; Hu, H.; Zhang, J.; Lv, S.; Yu, Y.; Wei, F.; Qin, T.; Xu, H.; Liu, Z.; Cui, G. *Chem. Mater.* 2014, **26**, 1485.
(191) Eperon, G. E.; Stranks, S. D.; Menelaou, C.; Johnston, M. B.; Herz, L. M.; Snaith, H. J. *Energy. Environ. Sci.* 2014, **7**, 982.
(192) Stoumpos, C. C.; Malliakas, C. D.; Kanatzidis, M. G. *Inorg. Chem..* 2013, **52**, 9019.
(193) Lee, J. W.; Seol, D. J.; Cho, A. N.; Park, N. G. *Adv. Mater.* 2014, **26**, 4991.
(194) Pellet, N.; Gao, P.; Gregori, G.; Yang, T. Y.; Nazeeruddin, M. K.; Maier, J.; Grätzel, M. *Angew. Chem. Int. Ed.* 2014, **53**, 3151.
(195) Lv, S.; Pang, S.; Zhou, Y.; Padture, N. P.; Hu, H.; Wang, L.; Zhou, X.; Zhu, H.; Zhang, L.; Huang, C.; Cui, G. *Phys. Chem. Chem. Phys.* 2014, **16**, 19206.
(196) Hanusch, F. C.; Wiesenmayer, E.; Mankel, E.; Binek, A.; Angloher, P.; Fraunhofer, C.; Giesbrecht, N.; Feckl, J. M.; Jaegermann, W.; Johrendt, D.; Bein, T.; Docampo, P. *J. Phys. Chem. Lett.* 2014, **5,** 2791
(197) Bernal, C.; Yang, K. *J. Phys. Chem. C* 2014, **118**, 24383.
(198) Ogomi, Y.; Morita, A.; Tsukamoto, S.; Saitho, T.; Fujikawa, N.; Shen, Q.; Toyoda, T.; Yoshino, K.; Pandey, S. S.; Ma, T.; Hayase, S. *J. Phys. Chem. Lett.* 2014, **5**, 1004.
(199) Hao, F.; Stoumpos, C. C.; Chang, R. P.; Kanatzidis, M. G. *J. Am. Chem. Soc.* 2014, **136**, 8094.
(200) Zuo, F.; Williams, S. T.; Liang, P. W.; Chueh, C. C.; Liao, C. Y.; Jen, A. K. *Adv. Mater.* 2014, **26**, 6454.
(201) Noel, N. K.; Stranks, S. D.; Abate, A.; Wehrenfennig, C.; Guarnera, S.; Haghighirad, A.-A.; Sadhanala, A.; Eperon, G. E.; Pathak, S. K.; Johnston, M. B.; Petrozza, A.; Herz, L. M.; Snaith, H. J. *Energy. Environ. Sci.* 2014, **7**, 3061.
(202) Hao, F.; Stoumpos, C. C.; Cao, D. H.; Chang, R. P. H.; Kanatzidis, M. G. *Nat. Photonics* 2014, **8**, 489.
(203) Mahmood, K.; Swain, B. S.; Kirmani, A. R.; Amassian, A. *J. Mater. Chem. A* 2014. **DOI:** 10.1039/C4TA04883K
(204) Oh, L. S.; Kim, D. H.; Lee, J. A.; Shin, S. S.; Lee, J.-W.; Park, I. J.; Ko, M. J.; Park, N.-G.; Pyo, S. G.; Hong, K. S.; Kim, J. Y. *J. Phys. Chem. C* 2014, **118**, 22991.
(205) Bera, A.; Wu, K.; Sheikh, A.; Alarousu, E.; Mohammed, O. F.; Wu, T. *J. Phys. Chem. C* 2014, **118**, 28494
(206) Eperon, G. E.; Burlakov, V. M.; Goriety, A.; Snaith, H. J. *ACS Nano*, 2014, **8**, 591
(207) Chen, P.-Y.; Qi, J.; Klug, M. T.; Dang, X.; Hammond, P. T.; Belcher, A. M. *Energy. Environ. Sci.* 2014. **7**, 3659
(208) Horvath, E.; Spina, M.; Szekrenyes, Z.; Kamaras, K.; Gaal, R.; Gachet, D.; Forro, L. *Nano Lett.* 2014. **DOI:** 10.1021/nl5020684

(209) Kang, S. M.; Ahn, N.; Lee, J.-W.; Choi, M.; Park, N.-G. *J. Mater. Chem. A* 2014, **2**, 20017.
(210) Kim, B. J.; Kim, D. H.; Lee, Y.-Y.; Shin, H.-W.; Han, G. S.; Hong, J. S.; Mahmood, K.; Ahn, T. K.; Joo, Y.-C.; Hong, K. S.; Park, N.-G.; Lee, S.; Jung, H. S. *Energy. Environ. Sci.* 2014. **DOI:** 10.1039/C4EE02441A
(211) Matteocci, F.; Razza, S.; Di Giacomo, F.; Casaluci, S.; Mincuzzi, G.; Brown, T. M.; D'Epifanio, A.; Licoccia, S.; Di Carlo, A. *Phys. Chem. Chem. Phys.* 2014, **16**, 3918.
(212) Qiu, L.; Deng, J.; Lu, X.; Yang, Z.; Peng, H. *Angew. Chem. Int. Ed.* 2014. **53**, 10425.
(213) Roldán-Carmona, C.; Malinkiewicz, O.; Betancur, R.; Longo, G.; Momblona, C.; Jaramillo, F.; Camacho, L.; Bolink, H. J. *Energy. Environ. Sci.* 2014, **7**, 2968.
(214) Chen, C.; Hsiao, S.; Chen, C.; Kang, H.; Huang, Z.; Lin, H. *J. Mater. Chem. A* **DOI:** 10.1039/C4TA05237D

TOC